AIAA JOURNAL
Vol. 55, No. 8, August 2017

# Development of an Aeroelastic Formulation for Deformable Airfoils Using Orthogonal Polynomials

Weihua Su*
*University of Alabama, Tuscaloosa, Alabama 35487-0280*

DOI: 10.2514/1.J055665

**In this paper, an aeroelastic formulation is developed to analyze aeroelastic behavior of flexible airfoils with arbitrary camber deformations. The camberwise bending deformation of flexible airfoils, described by using the orthogonal Legendre polynomials, is considered in addition to traditional rigid-body plunging and pitching motions. The complete set of aeroelastic equations of motion is derived by following Hamilton's principle, where a two-dimensional finite-state unsteady aerodynamic theory is applied to calculate the aerodynamic loads of flexible airfoils with both rigid-body motions and arbitrary camber deformations. The finite-state aerodynamic theory is also modified to involve magnitudes of the Legendre polynomials in the aerodynamic load equations. The aeroelastic equations, featuring rigid-body motions and camber deformation magnitudes as independent degrees of freedom, may facilitate the analysis of camber effects on aeroelastic characteristics of flexible airfoils. Numerical studies of this paper validate the developed aerodynamic and aeroelastic formulations by comparison with other published research and computational results. Finally, the impacts of camber flexibility on static and dynamic aeroelastic characteristics of flexible airfoils are explored.**



## Nomenclature

| | | |
|---|---|---|
| $A$ | = | state-space system matrix of aeroelastic system |
| $a$ | = | dimensionless location of elastic axis, $d/b$ |
| $b$ | = | semichord of airfoil, m |
| $\bar{b}$ | = | coefficients for inflow states |
| $\tilde{C}$ | = | aeroelastic damping matrix |
| $d$ | = | distance of midchord point in front of elastic axis, m |
| $E, F_1, F_2, F_3$ | = | coefficients for inflow equation |
| $EI$ | = | chordwise bending rigidity of airfoil, N · m |
| $h$ | = | camber deformation of airfoil, m |
| $h_n$ | = | Glauert expansion of camber deformation of airfoil, m |
| $I_\alpha$ | = | mass moment of inertia of airfoil, kg · m |
| $I_\eta$ | = | camberwise inertia of airfoil, kg/m |
| $\tilde{K}$ | = | aeroelastic stiffness matrix |
| $K_\alpha$ | = | torsional spring constant per unit span, N |
| $K_\eta$ | = | camberwise rigidity of airfoil, N/m$^2$ |
| $\mathcal{K}_\eta$ | = | equivalent camberwise rigidity of airfoil due to coupling with plunging, N/m$^2$ |
| $K_\xi$ | = | linear spring constant per unit span, N/m$^2$ |
| $K_{\xi\eta}$ | = | coupled rigidity of airfoil between plunging and camber deformation, N/m$^2$ |
| $\mathcal{L}$ | = | aerodynamic lift on airfoil, N/m |
| $\mathcal{L}_n$ | = | generalized aerodynamic loads, N/m |
| $\mathcal{M}$ | = | aerodynamic moment on airfoil, N |
| $\tilde{M}$ | = | aeroelastic inertia matrix |
| $m$ | = | total mass of airfoil, kg/m |
| $\hat{m}$ | = | mass per unit chordwise length of airfoil, kg/m$^2$ |
| $N$ | = | number of inflow states defined on airfoil |
| $\mathcal{N}$ | = | camberwise aerodynamic loads on airfoil, N/m |
| $P_i$ | = | Legendre polynomials, $i = 0, 1, 2, 3, \ldots$ |
| $p$ | = | aerodynamic pressure, Pa |
| $q$ | = | dynamic pressure, N/m$^2$ |
| $r_\alpha$ | = | dimensionless radius of gyration |
| $r_1, r_2, r_3$ | = | ratios between different rigidity entries in static aeroelastic analysis |
| $S_\alpha$ | = | structural imbalance of airfoil, kg |
| $s$ | = | matrix relating Legendre polynomials and Chebyshev polynomials |
| $\mathcal{T}$ | = | kinetic energy of airfoil, J/m |
| $T_i$ | = | Chebyshev polynomials of the first kind, $i =, 1, 2, 3, \ldots$ |
| $\mathcal{U}$ | = | potential energy of airfoil, J/m |
| $U_f$ | = | flutter boundary, m/s |
| $U_0$ | = | freestream velocity, m/s |
| $u_n$ | = | Glauert expansion of airfoil horizontal velocity, m/s |
| $v_n$ | = | Glauert expansion of airfoil vertical velocity, m/s |
| $\mathcal{W}$ | = | external work on airfoil, J/m |
| $x_\alpha$ | = | dimensionless location of center of gravity |
| $\alpha$ | = | rigid-body pitching of airfoil, rad |
| $\alpha^0$ | = | zero lift line angle, rad |
| $\alpha_0$ | = | pitching angle when torsional spring is unstretched, rad |
| $\eta$ | = | magnitude of Legendre polynomials, m |
| $\lambda$ | = | inflow states, m/s |
| $\lambda_0$ | = | inflow velocities, m/s |
| $\xi$ | = | rigid-body plunging of airfoil, m |
| $\rho$ | = | air density, kg/m$^3$ |
| $\omega_\alpha$ | = | airfoil nominal natural frequency of pitching, rad/s |
| $\omega_\eta$ | = | airfoil nominal natural frequency of first bending, rad/s |
| $\omega_\xi$ | = | airfoil nominal natural frequency of plunging, rad/s |

Presented as Paper 2016-2048 at the 15th Dynamics Specialists Conference, San Diego, CA, 4–8 January 2016; received 7 September 2016; revision received 30 January 2017; accepted for publication 4 February 2017; published online 26 April 2017. 

*Assistant Professor, Department of Aerospace Engineering and Mechanics; suw@eng.ua.edu. Senior Member AIAA.

## I. Introduction

AT THE advent of recent developments in advanced composites as well as sensor and actuator technologies, in-flight adaptive wing morphing is now becoming a tangible goal. With the morphing technologies, wing and aircraft performances (e.g., aerodynamic drag, flight range, endurance, maneuverability, gust rejection, etc.) can be passively or actively tailored according to a wide range of flight conditions, while maintaining the flight stability. Traditionally, discrete control surfaces were used to redistribute the aerodynamic loads along the wingspan during the flight, so as to tailor the aircraft

performance. However, the deflection of discrete surfaces, while providing the desired lift control, may increase the aerodynamic drag. To address this issue, different techniques had been applied to explore more efficient approaches to control the wing loading, improve the aircraft performance, and reduce the drag. An effective alternative has been to introduce conformal wing/airfoil shape changes for the aerodynamic load control. Advantages may be gained with the camber variations along the wingspan [1] (e.g., adaptive redistribution of the wing loads, reduced wing root bending moments, reduced drag, etc.). FlexSys, Inc., with the support from the U.S. Air Force Research Laboratory (AFRL), developed a compliant trailing-edge concept in their Mission Adaptive Compliant Wing (MACW) project [2]. With a piezoelectric actuator driving the compliant morphing mechanism, it was shown that the continuous wing trailing edge was able to deflect about $\pm 10$ deg [3]. In Bilgen et al. [4], a cantilever wing platform was designed and experimentally tested for the camber changes with active piezoelectric actuations. In rotorcraft application, the optimal airfoil design was studied for the control of airfoil camber [5]. Recently, in an effort to achieve a low-drag, high-lift configuration, a flexible transport aircraft wing using the variable camber continuous trailing-edge flaps (VCCTEF) to vary the wing camber is being studied at NASA Ames Research Center. The studies showed that the highly flexible wing, if elastically shaped in-flight by active control of wing twist and bending, may improve aerodynamic efficiency through reduced drag during cruise and enhanced lift performance during takeoff and landing [6]. Nguyen and Ting [7] identified the flutter characteristics of the wing using a linear beam formulation and vortex-lattice aerodynamics. Their study also indicated the reduction of flutter boundary of the wing with increased structural flexibility.

Aerodynamic characteristics and the potential performance enhancement of deformable airfoils have been studied in the literature (e.g., [8–11]). These studies usually considered the impact of the airfoil's flexibility on the aerodynamic loads on the airfoil segment. Computational fluid dynamics (CFD) tools were applied to study the wing camber effects (e.g., Swanson and Isaac [12]), where the detailed flow condition around the cambered airfoil was captured. However, these CFD solutions may be very computationally expensive. Another solution with medium fidelity is to employ panel methods to solve the unsteady aerodynamics of cambered wings. The unsteady vortex-lattice method (e.g., [13,14]) can be easily adopted to consider the wing camber change. This is particularly feasible in the analysis of membrane wings [13], where the airfoil camber shape significantly impacts the aerodynamic loads generated on the wing and thus the aeroelastic behavior. The panel method has the advantage in that it naturally models the aerodynamic loads due to the airfoil/wing camber change. However, a shell-based structural model that can naturally consider the camber deformation is needed in further aeroelastic studies to fully take advantage of the panel method, which in turn may increase the dimension of the problem. On the other hand, two-dimensional (2-D) aerodynamic models are also viable for the purpose of quantifying the aerodynamic loads of flexible airfoils, provided that they properly consider the camber deformation of the airfoils. By using the strip theory, aerodynamic loads on a complete slender wing can be efficiently estimated, which may be further applied to study its aeroelastic characteristics (e.g., divergence, flutter, and transient response) with camberwise degrees of freedom.

Furthermore, aeroelastic characteristics airfoils and wings with camberwise flexibility are also of importance to study. The camber effects on the wing aeroelastic behavior lie in two aspects. For models with a fixed wing box, whereas the leading or trailing edge of the wing is flexible and morphing, such as the MACW [2], the wing with VCCTEF [6], and the variable camber compliant wing designed in AFRL [15,16], the aforementioned aerodynamic impact is dominant, whereas the wing structural dynamic characteristic remains almost unchanged. Therefore, the aeroelastic behavior of the wing can be accurately captured as long as the camber effect is properly modeled in the aerodynamics. However, for more complicated wings, such as membrane wings or actively actuated wings, the camber effect also significantly impacts their structural dynamic behavior. In these cases, the structural model should be properly chosen to be coupled with the aerodynamics. Obviously, the second problem involves richer aeroelastic phenomena. Seber and Sakarya [17] performed nonlinear modeling and static aeroelastic analysis of an adaptive camber wing. However, their study did not cover dynamic responses of the wing. Murua et al. [18] studied the dynamic aeroelasticity of a compliant airfoil, with a focus on the flutter analysis. Cook and Smith [19] instead used the CFD (FUN3D) approach in the aeroelastic analysis of a flexible airfoil. In these studies, the camber deformation of the flexible airfoil was both modeled as an assumed symmetric parabolic bending profile [20]. However, the actual camber deformation of a morphing wing (such as the wings studied in [6,7]) may be complicated. An assumed symmetric bending profile may not be enough to represent the actual camber shape and the resulting aerodynamic loads on the airfoil. Kumar and Cesnik [21] improved the approximation of airfoil camber deformation by applying both parabolic and cubic functions. A dynamic stall model was used to evaluate and optimize the aeroelastic performance of cambered helicopter blades. For more accurate analysis, an aeroelastic formulation that allows for arbitrary wing camber deformations is still necessary.

To this end, an aeroelastic formulation will be developed for flexible airfoils with the capability of modeling their arbitrary camber deformations. Such camber deformations will be included in both the structural and aerodynamic equations. Specifically, the Legendre polynomials [22,23], a set of complete and orthogonal functions defined along the chord, will be used to represent the airfoil camber deformation. This is essentially a Ritz approximation of the camber deformation. The structural dynamic equations of flexible airfoils with both rigid-body motions and camber deformations will be coupled with the unsteady finite-state inflow aerodynamics [24], where a Glauert expansion will be used to account for the airfoil deformation in the calculation of aerodynamic loads. The aeroelastic equations will be transformed into the state-space form to facilitate the stability analysis. Finally, numerical studies of this paper will demonstrate the applicability of the aeroelastic formulation in static and dynamic aeroelastic analyses of flexible airfoils.

## II. Theoretical Formulation

In this section, the aeroelastic equations of motion for flexible airfoils are derived by following Hamilton's principle. The unsteady finite-state inflow aerodynamic formulation considering arbitrary airfoil deformations is coupled with the structural dynamic equations. Specially, the Legendre polynomials are introduced to represent the airfoil's arbitrary camberwise deformation that is integrated with the classic rigid-body plunging and pitching motions of the airfoil. Details of the theoretical formulation are provided as follows.

### A. Flexible Airfoils with Arbitrary Camber Deformation

As shown in Fig. 1, the camber deformation $h$ (positive displacement down) is considered for a flexible airfoil, in addition to the plunging $\xi$ (positive down) and pitching $\alpha$ (positive nose up) motions that a rigid airfoil also has. The airfoil's displacement due to the rigid-body motions and arbitrary camber deformation is written in terms of a set of trial functions, given as

$$\begin{aligned}\xi(t) + x\alpha(t) + h(x,t) &= P_0(x)\eta_0(t) + P_1(x)\eta_1(t) + P_2(x)\eta_2(t) + P_3(x)\eta_3(t) \\ &+ P_4(x)\eta_4(t) + \cdots \end{aligned} \tag{1}$$

where $\eta_i$ are the magnitudes of the associated trial functions $P_i$. The Legendre polynomials, a set of complete and orthogonal polynomials defined in the domain of $[-b, b]$, are used in the current study to represent the airfoil's rigid-body motions and camber deformation. They are defined by

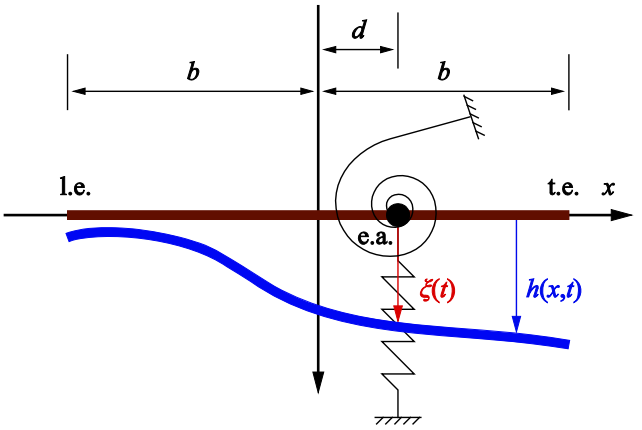


**Fig. 1 Rigid-body motions and arbitrary camber deformation of a flexible airfoil.**

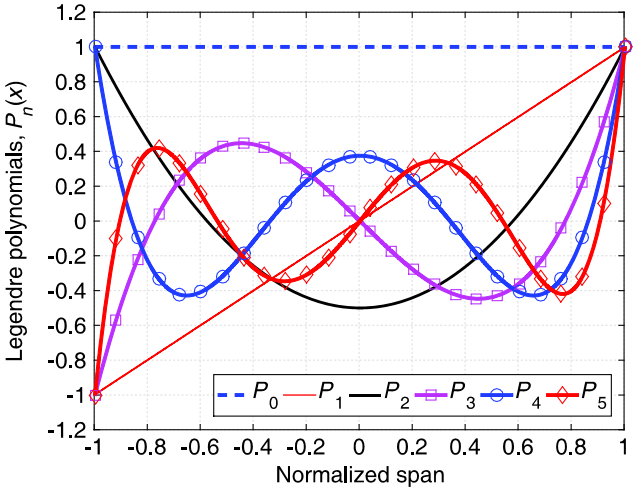


**Fig. 2 First six Legendre polynomials with $x$ coordination normalized by $b$.**

$$P_0(x) = 1, \qquad P_1(x) = \frac{x}{b},$$
$$P_{j+1}(x) = \frac{(2j+1)(x/b)P_j(x) - jP_{j-1}(x)}{j+1}, \qquad j = 1, 2, 3, \ldots \tag{2}$$

with Fig. 2 illustrating the first six Legendre polynomials. In fact, any arbitrary function defined on $[-b, b]$ can be represented as a combination of the Legendre polynomials given in Eq. (2). When comparing both sides of Eq. (1), one can find polynomials $P_0$ and $P_1$ represent the airfoil's rigid-body plunging and pitching motions (see Fig. 2), respectively, where their magnitudes are

$$\eta_0(t) = \xi(t), \quad \eta_1(t) = b\alpha(t) \tag{3}$$

Therefore, $P_0$ and $P_1$ are actually not necessary for modeling pure elastic camber deformations of a flexible airfoil. This leads to

$$h(x,t) = P_2(x)\eta_2(t) + P_3(x)\eta_3(t) + P_4(x)\eta_4(t) + \cdots = \sum_{i=2}^{\infty} P_i(x)\eta_i(t) = \{P(x)\}\{\eta(t)\} \tag{4}$$

It is of interest to point out that Palacios and Cesnik [20] and Murua et al. [18] used one assumed finite-section mode to approximate the camber deformation of a flexible airfoil, which was given as

$$\Psi(x) = \left(\frac{x}{b}\right)^2 - \frac{1}{3} \tag{5}$$

It differs from polynomial $P_2$ only by a coefficient of $3/2$. Therefore, $P_2$ can also be considered a finite-section mode of the airfoil. However, the formulation to be developed herein enables one to model any camber deformations of flexible airfoils by including more Legendre polynomials.

Note that $\eta_i$ are usually solved from the equations of motion of the flexible airfoil. However, for inverse problems where the camber deformation of the airfoil is known, the magnitudes of Legendre polynomials can be determined by the following integral:

$$\eta_i(t) = \frac{2i+1}{2b}\int_{-b}^{b} h(x,t)P_i(x)\,\mathrm{d}x \tag{6}$$

### B. Structural Dynamic Equations of Flexible Airfoils

A flexible airfoil is considered as a nonuniform beam in bending when its equations of motion are developed. The rigid-body motions are measured at the point where the linear and torsional springs are attached (see Fig. 1). The kinetic energy $\mathcal{T}$, potential energy $\mathcal{U}$, and external work $\mathcal{W}$ of a flexible airfoil are

$$\mathcal{T}(t) = \int_{-b}^{b} \frac{1}{2}\hat{m}(x)\left[\dot{\xi}(t) + (x-d)\dot{\alpha}(t) + \dot{h}(x,t)\right]^2 \mathrm{d}x$$
$$\mathcal{U}(t) = \frac{1}{2}K_\xi\left(\xi(t) + h(d,t)\right)^2 + \frac{1}{2}K_\alpha\left(\alpha(t) - \alpha_0\right)^2 + \int_{-b}^{b}\frac{1}{2}EI(x)(h''(x,t))^2\,\mathrm{d}x$$
$$\mathcal{W}(t) = \int_{-b}^{b} -\Delta p(x,t)[\xi(t) + (x-d)\alpha(t) + h(x,t)]\,\mathrm{d}x + \int_{-b}^{b}\hat{m}(x)g[\xi(t) + (x-d)\alpha(t) + h(x,t)]\,\mathrm{d}x \tag{7}$$

where $d$ is the distance of the midchord in front of the elastic axis (e.a.) (where the two springs are attached to the airfoil), $\hat{m}$ is the mass of the airfoil per unit chordwise length, $K_\xi$ is the linear spring constant per unit wingspan, $K_\alpha$ is the torsional spring constant per unit wingspan, $EI$ is the chordwise bending rigidity of the airfoil, $\Delta p$ is the aerodynamic pressure difference between the bottom and top surfaces of the airfoil, and $\alpha_0$ is the pitching angle when the torsional spring is not stretched. The overdot denotes the time derivative, whereas the double prime denotes the second spatial partial derivative of the corresponding variable. The following quantities are defined to simplify the notations:

$$m = \int_{-b}^{b}\hat{m}(x)\,\mathrm{d}x, \qquad S_\alpha = \int_{-b}^{b}\hat{m}(x)(x-d)\,\mathrm{d}x,$$
$$I_\alpha = \int_{-b}^{b}\hat{m}(x)\left(x-d\right)^2\mathrm{d}x \tag{8}$$

where $m$, $S_\alpha$, and $I_\alpha$ are the total mass, structural imbalance, and mass moment of inertia of the airfoil in pitching, respectively. The aerodynamic lift $\mathcal{L}$ (positive up) and moment $\mathcal{M}$ (positive nose up) acting on the airfoil are calculated by the integrals of the pressure difference across the airfoil surfaces:

$$\mathcal{L}(t) = \int_{-b}^{b}\Delta p(x,t)\,\mathrm{d}x, \quad \mathcal{M}(t) = -\int_{-b}^{b}\Delta p(x,t)(x-d)\,\mathrm{d}x \tag{9}$$

Because no lead–lag motion of the airfoil is involved, aerodynamic drag is not considered in the formulation.

By following Hamilton's principle, the equations of motion of flexible airfoils are derived as

$$\begin{bmatrix} m & S_\alpha & 0 \\ S_\alpha & I_\alpha & 0 \\ 0 & 0 & I_\eta \end{bmatrix} \begin{Bmatrix} \ddot{\xi}(t) \\ \ddot{\alpha}(t) \\ \ddot{\eta}(t) \end{Bmatrix} + \begin{bmatrix} K_\xi & 0 & K_{\xi\eta} \\ 0 & K_\alpha & 0 \\ K_{\xi\eta}^T & 0 & K_\eta + \mathcal{K}_\eta \end{bmatrix} \begin{Bmatrix} \xi(t) \\ \alpha(t) \\ \eta(t) \end{Bmatrix} = \begin{Bmatrix} -\mathcal{L}(t) + mg \\ \mathcal{M}(t) + S_\alpha g + K_\alpha \alpha_0 \\ \mathcal{N}(t) + Hg \end{Bmatrix} \tag{10}$$

where

$$\begin{aligned} [I_\eta] &= \int_{-b}^{b} \{P(x)\}^T \hat{m}(x) \{P(x)\}\, \mathrm{d}x \\ [K_\eta] &= \int_{-b}^{b} \{P''(x)\}^T EI(x) \{P''(x)\}\, \mathrm{d}x \\ \{K_{\xi\eta}\} &= K_\xi \{P(d)\} \\ [\mathcal{K}_\eta] &= \{P(d)\}^T K_\xi \{P(d)\} \\ \{\mathcal{N}(t)\} &= \int_{-b}^{b} -\{P(x)\}^T \Delta p(x,t)\, \mathrm{d}x \\ \{H\} &= \int_{-b}^{b} \{P(x)\}^T \hat{m}(x)\, \mathrm{d}x \end{aligned} \tag{11}$$

Note that the coupling between the rigid-body motions and the camber deformation is neglected when the variation of the kinetic energy is calculated. Otherwise, the inertial matrix in Eq. (10) is fully populated. In addition, the dimension of camber degrees of freedom $\eta$ is infinitive, and so are those of camber inertia $I_\eta$, stiffness components $K_{\xi\eta}$, $K_\eta$, and $\mathcal{K}_\eta$, and loads $\mathcal{N}$ and $Hg$. However, one may approximate the camber deformation by truncating the series of Legendre polynomials. For simplicity, those quantities varying in time will not be explicitly written as time functions in the following derivation.

### C. Unsteady Aerodynamics

Unsteady aerodynamic loads in this study are derived based on the 2-D finite-state formulation for thin airfoils presented in Peters and Johnson [24]. A Glauert expansion is performed on the potential flow equations. The generalized aerodynamic loads on an airfoil are obtained through the Glauert expansion of the aerodynamic pressure difference

$$\mathcal{L}_n = -\int_{-b}^{b} \Delta p(x) T_n(x)\, \mathrm{d}x \tag{12}$$

where $T_n(x)$ are the Chebyshev polynomials of the first kind. The matrix form of Eq. (12) is given as [24]

$$\frac{\{\mathcal{L}_n\}}{2\pi\rho} = -b^2[M]\{\ddot{h}_n + \dot{v}_n\} - bu_0[C]\{\dot{h}_n + v_n - \lambda_0\} - u_0^2[K]\{h_n\} - b[G]\{\dot{u}_0 h_n - u_0 v_n + u_0 \lambda_0\} \tag{13}$$

where

$$\{v_n\} = \begin{Bmatrix} v_0 \\ v_1 \\ 0 \\ \vdots \end{Bmatrix} = \begin{Bmatrix} U_0\alpha + \dot{\xi} - d\dot{\alpha} \\ b\dot{\alpha} \\ 0 \\ \vdots \end{Bmatrix},$$

$$\{\dot{v}_n\} = \begin{Bmatrix} \dot{v}_0 \\ \dot{v}_1 \\ 0 \\ \vdots \end{Bmatrix} = \begin{Bmatrix} U_0\dot{\alpha} + \ddot{\xi} - d\ddot{\alpha} \\ b\ddot{\alpha} \\ 0 \\ \vdots \end{Bmatrix}, \quad \{\lambda_0\} = \begin{Bmatrix} \lambda_0 \\ 0 \\ 0 \\ \vdots \end{Bmatrix},$$

$$u_0 = U_0 \tag{14}$$

The aerodynamic matrices $[M]$, $[C]$, $[K]$, and $[G]$ are all defined in Peters and Johnson [24]. The inflow parameter $\lambda_0$ accounts for induced flow due to the free vorticity, which is the weighted summation of the inflow states $\lambda$ as described in Peters and Johnson [24]:

$$\lambda_0 = \frac{1}{2}\sum_{j=1}^{N} \bar{b}_j \lambda_j \tag{15}$$

where $N$ is the number of inflow states defined on the airfoil. The inflow states are governed by

$$[E]\{\dot{\lambda}\} + \frac{U_0}{b}\{\lambda\} = \{c\}\left[U_0\dot{\alpha} + \ddot{\xi} + \left(\frac{1}{2}b - d\right)\ddot{\alpha}\right] \tag{16}$$

where the coefficients $\bar{b}$, $E$, and $c$ are all defined in Peters et al. [25].

In Eq. (13), $h_n$ are the Glauert expansion coefficients of the camber deformation $h(x)$ [24], such that

$$h(x) = \sum_{n=0}^{\infty} T_n(x) h_n = T_0(x)h_0 + T(x)_1 h_1 + T_2(x)h_2 + \cdots \tag{17}$$

However, $h(x)$ has already been represented by the Legendre polynomials in the structural dynamic modeling, as shown in Eq. (4). Therefore, to obtain the Glauert expansion coefficients of $h(x)$, one only needs to find the Glauert expansion of the Legendre polynomials, that is,

$$\begin{aligned} h(x) &= \sum_{i=2}^{\infty} P_i(x)\eta_i = \sum_{i=2}^{\infty}\left[\sum_{n=0}^{\infty} T_n(x) s_{ni}\right]\eta_i \\ &= \sum_{n=0}^{\infty}\left(T_n(x)\left[\sum_{i=2}^{\infty} s_{ni}\eta_i\right]\right) \end{aligned} \tag{18}$$

where each Legendre polynomial is expanded and $s_{ni}$ are the Glauert expansion coefficients of the $i$th Legendre polynomial. From Eqs. (17) and (18), it is simple to have

$$h_n = \sum_{i=2}^{\infty} s_{ni}\eta_i \tag{19}$$

where $[s]$ has infinitive dimensions. Its first few entries are given by

$$[s] = \begin{bmatrix} 1/4 & 0 & 9/64 & 0 & 250/2560 & 0 & \\ 0 & 3/8 & 0 & 30/128 & 0 & \ddots & \\ 3/4 & 0 & 20/64 & 0 & 525/2560 & 0 & \\ 0 & 5/8 & 0 & 35/128 & 0 & \ddots & \\ 0 & 0 & 35/64 & 0 & 630/2560 & 0 & \\ 0 & 0 & 0 & 63/128 & 0 & \ddots & \\ 0 & 0 & 0 & 0 & 1155/2560 & 0 & \\ 0 & 0 & 0 & 0 & 0 & \ddots & \end{bmatrix} \tag{20}$$

Substituting Eq. (19) into Eq. (13) yields the generalized aerodynamic loads written in terms of the magnitudes of the Legendre polynomials $\eta$:

$$\frac{\{\mathcal{L}_n\}}{2\pi\rho} = -b^2[M]\left\{\sum_{i=2}^{\infty} s_{ni}\ddot{\eta}_i + \dot{v}_n\right\} - bu_0[C]\left\{\sum_{i=2}^{\infty} s_{ni}\dot{\eta}_i + v_n - \lambda_0\right\} - u_0^2[K]\left\{\sum_{i=2}^{\infty} s_{ni}\eta_i\right\} - b[G]\left\{\dot{u}_0\sum_{i=2}^{\infty} s_{ni}\eta_i - u_0 v_n + u_0\lambda_0\right\} \tag{21}$$

Therefore, the individual generalized aerodynamic loads $\mathcal{L}_n$ can be obtained from Eq. (21) based on the input of airfoil motions ($\xi$, $\alpha$, and $\eta$) and their time derivatives. $\mathcal{L}_n$ are then used to calculate the resultant aerodynamic loads on the airfoil. Actually, the first two integrals of Eq. (12) result in the aerodynamic lift and moment on the airfoil

$$\begin{aligned}\mathcal{L} &= \int_{-b}^{b} \Delta p(x)\,\mathrm{d}x = \int_{-b}^{b} \Delta p(x) T_0(x)\,\mathrm{d}x = -\mathcal{L}_0 \\ \mathcal{M} &= -\int_{-b}^{b} \Delta p(x)(x-d)\,\mathrm{d}x \\ &= d\int_{-b}^{b} \Delta p(x) T_0(x)\,\mathrm{d}x - b\int_{-b}^{b} \Delta p(x) T_1(x)\,\mathrm{d}x \\ &= -dL_0 + b\mathcal{L}_1 \end{aligned} \tag{22}$$

The camber loads $\mathcal{N}$ are obtained from the integrations of the pressure difference $\Delta p$ weighted by the Legendre polynomials, as shown in Eq. (11). They are further related to the Glauert expansion of $\Delta p$ (i.e., the integrations of $\Delta p$ weighted by the Chebyshev polynomials). The first few entries of $\mathcal{N}$ are given by

$$\{\mathcal{N}\} = \begin{Bmatrix} \frac{1}{4}\mathcal{L}_0 + \frac{3}{4}\mathcal{L}_2 \\ \frac{3}{8}\mathcal{L}_1 + \frac{5}{8}\mathcal{L}_3 \\ \frac{9}{64}\mathcal{L}_0 + \frac{20}{64}\mathcal{L}_2 + \frac{35}{64}\mathcal{L}_4 \\ \frac{30}{128}\mathcal{L}_1 + \frac{35}{128}\mathcal{L}_3 + \frac{63}{128}\mathcal{L}_5 \\ \vdots \end{Bmatrix} = [s]^T\{\mathcal{L}_n\} \tag{23}$$

To summarize, Eqs. (22) and (23) give the complete set of aerodynamic loads on a flexible airfoil. It is clear from Eq. (12) that the potential flow-based aerodynamics does not consider friction drag due to the viscous effects, unless some ad hoc corrections (e.g., by using XFoil's calculation) are applied.

### D. Aeroelastic Equations and Flutter Boundary of Flexible Airfoil

Equations (10) and (16) complete the aeroelastic governing equations of a flexible airfoil, which are

$$\begin{aligned}&\begin{bmatrix} m & S_\alpha & 0 \\ S_\alpha & I_\alpha & 0 \\ 0 & 0 & I_\eta \end{bmatrix}\begin{Bmatrix} \ddot{\xi} \\ \ddot{\alpha} \\ \ddot{\eta} \end{Bmatrix} + \begin{bmatrix} K_\xi & 0 & K_{\xi\eta} \\ 0 & K_\alpha & 0 \\ K_{\xi\eta}^T & 0 & K_\eta + \mathcal{K}_\eta \end{bmatrix}\begin{Bmatrix} \xi \\ \alpha \\ \eta \end{Bmatrix} \\ &= \begin{Bmatrix} -\mathcal{L} + mg \\ \mathcal{M} + S_\alpha g + K_\alpha \alpha_0 \\ \mathcal{N} + Hg \end{Bmatrix} \\ &[E]\{\dot{\lambda}\} = [F_1]\{\lambda\} + [F_2]\begin{Bmatrix} \ddot{\xi} \\ \ddot{\alpha} \\ \ddot{\eta} \end{Bmatrix} + [F_3]\begin{Bmatrix} \dot{\xi} \\ \dot{\alpha} \\ \dot{\eta} \end{Bmatrix} \end{aligned} \tag{24}$$

where

$$[F_1] = -\frac{U_0}{b}[I], \quad [F_2] = \begin{bmatrix} \{c\} & \left(\frac{1}{2}b - d\right)\{c\} & [0] \end{bmatrix}, \quad [F_3] = \begin{bmatrix} \{0\} & U_0\{c\} & [0] \end{bmatrix} \tag{25}$$

Obviously, it is assumed that the inflow states are independent of the camber deformations. The transient aeroelastic analysis of the flexible airfoil can be performed by using numerical integration of Eq. (24). To perform the flutter analysis, one needs to expand the aerodynamic loads on the right-hand side of Eq. (24) with respect to the independent variables ($\xi$, $\alpha$, $\eta$, and $\lambda$) and group with the terms on the left-hand side, yielding

$$[\tilde{M}]\begin{Bmatrix} \ddot{\xi} \\ \ddot{\alpha} \\ \ddot{\eta} \end{Bmatrix} + [\tilde{C}]\begin{Bmatrix} \dot{\xi} \\ \dot{\alpha} \\ \dot{\eta} \end{Bmatrix} + [\tilde{K}]\begin{Bmatrix} \xi \\ \alpha \\ \eta \end{Bmatrix} = [D]\{\lambda\} + \{F_0\} \tag{26}$$

where the aeroelastic inertial, damping, and stiffness matrices are

$$\begin{aligned}[\tilde{M}] &= \begin{bmatrix} m & S_\alpha & 0 \\ S_\alpha & I_\alpha & 0 \\ 0 & 0 & I_\eta \end{bmatrix} - \begin{bmatrix} -\mathcal{L}_{\ddot{\xi}} & -\mathcal{L}_{\ddot{\alpha}} & -\mathcal{L}_{\ddot{\eta}} \\ \mathcal{M}_{\ddot{\xi}} & \mathcal{M}_{\ddot{\alpha}} & \mathcal{M}_{\ddot{\eta}} \\ \mathcal{N}_{\ddot{\xi}} & \mathcal{N}_{\ddot{\alpha}} & \mathcal{N}_{\ddot{\eta}} \end{bmatrix}, \\ [\tilde{C}] &= -\begin{bmatrix} -\mathcal{L}_{\dot{\xi}} & -\mathcal{L}_{\dot{\alpha}} & -\mathcal{L}_{\dot{\eta}} \\ \mathcal{M}_{\dot{\xi}} & \mathcal{M}_{\dot{\alpha}} & \mathcal{M}_{\dot{\eta}} \\ \mathcal{N}_{\dot{\xi}} & \mathcal{N}_{\dot{\alpha}} & \mathcal{N}_{\dot{\eta}} \end{bmatrix}, \\ [\tilde{K}] &= \begin{bmatrix} K_\xi & 0 & K_{\xi\eta} \\ 0 & K_\alpha & 0 \\ K_{\xi\eta}^T & 0 & K_\eta + \mathcal{K}_\eta \end{bmatrix} - \begin{bmatrix} -\mathcal{L}_\xi & -\mathcal{L}_\alpha & -\mathcal{L}_\eta \\ \mathcal{M}_\xi & \mathcal{M}_\alpha & \mathcal{M}_\eta \\ \mathcal{N}_\xi & \mathcal{N}_\alpha & \mathcal{N}_\eta \end{bmatrix}, \\ [D] &= \begin{bmatrix} -\mathcal{L}_\lambda \\ \mathcal{M}_\lambda \\ \mathcal{N}_\lambda \end{bmatrix}, \quad \{F_0\} = \begin{Bmatrix} mg \\ S_\alpha g + K_\alpha \alpha_0 \\ Hg \end{Bmatrix} \end{aligned} \tag{27}$$

In the preceding equations, $\mathcal{L}$, $\mathcal{M}$, and $\mathcal{N}$ with individual subscripts $\xi$, $\alpha$, $\eta$, and $\lambda$ means the partial derivatives of the loads with respect to the corresponding variables. The calculation of these partial derivatives is straightforward, because the aerodynamic loads have been derived as the explicit functions of the airfoil's rigid-body motions and camber degrees of freedom, as well as their time derivatives. Equation (26) can be further written into the state-space form as

$$\begin{bmatrix} I & 0 & 0 \\ 0 & \tilde{M} & 0 \\ 0 & F_2 & E \end{bmatrix}\{\dot{x}\} = \begin{bmatrix} 0 & I & 0 \\ -\tilde{K} & -\tilde{C} & D \\ 0 & F_3 & F_1 \end{bmatrix}\{x\} + \begin{Bmatrix} 0 \\ F_0 \\ 0 \end{Bmatrix} \tag{28}$$

where

$$\{x\}^T = \{\, \xi \quad \alpha \quad \eta^T \quad \dot{\xi} \quad \dot{\alpha} \quad \dot{\eta}^T \quad \lambda^T \,\} \tag{29}$$

The homogenous part of Eq. (28) is further simplified as

$$\dot{x} = Ax, \quad A = \begin{bmatrix} I & 0 & 0 \\ 0 & \tilde{M} & 0 \\ 0 & F_2 & E \end{bmatrix}^{-1}\begin{bmatrix} 0 & I & 0 \\ -\tilde{K} & -\tilde{C} & D \\ 0 & F_3 & F_1 \end{bmatrix} \tag{30}$$

Finally, the flutter boundary of the airfoil is searched by evaluating the eigenvalues of the system matrix $A$ within a range of freestream velocities. The unstable speed is identified when the real part of an eigenvalue turns to positive [26]. It is clear that the gravitational loads $mg$, $S_\alpha g$, and $Hg$ and the constant pitching angle $\alpha_0$ have no impact on the flutter instability, because they do not participate in the $A$ matrix. However, the relative position between c.g. and e.a. ($S_\alpha/mb$) may affect the airfoil's flutter characteristic. More details will be discussed in the next section.

## III. Numerical Studies

Several numerical results are presented in this section. First, the Legendre polynomials are used to approximate the camber line of a family of NACA four-digit airfoils with the same camber shape but different thicknesses. The resulting camber line geometry is fed into the developed aerodynamic equation to evaluate the aerodynamic

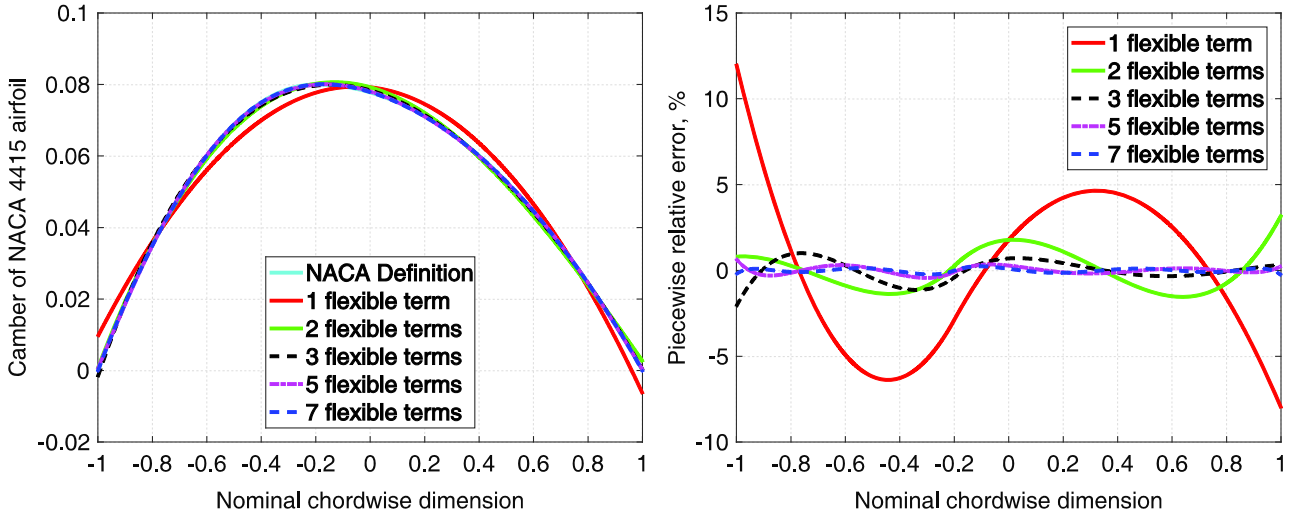


**a) Approximate camber line** **b) Piecewise error with respect to maximum camber**

**Fig. 3 Approximation of the camber line of NACA 4415 airfoil.**



loads of a cambered airfoil. Additionally, more discussions are focused on the static and dynamic characteristics of a flexible airfoil. Especially, the impact of the airfoil's camberwise rigidity and inertia on the aeroelastic system's divergence and flutter boundary are explored.

### A. Approximation of Camber Line Geometry and Aerodynamic Load of Cambered Airfoils

By definition, the camber line of a NACA four-digit airfoil is described by

$$y_c = \begin{cases} \frac{m_c}{p_c^2}[2p_c x_c - x_c^2] & 0 \le x_c \le p_c \\ \frac{m_c}{(1-p_c)^2}[1-2p_c + 2p_c x_c - x_c^2] & p_c \le x_c \le 1 \end{cases} \tag{31}$$

where $x_c$ is the chordwise coordinate ranging from zero to one, which can be transferred to the range of $[-1, 1]$. As an example, a family of NACA 44xx ("xx" denotes the maximum airfoil thickness) airfoils are used, where $m_c = 0.04$ and $p_c = 0.4$. A thin, flat airfoil is then bent to have the same camber shape as the NACA 44xx airfoils. Its aerodynamic loads with such a camber can be calculated using the formulation derived in the current study. Obviously, the series of the Legendre polynomials needs to be truncated when the camber line is approximated, where the magnitudes of the polynomials are found by using Eq. (6). In this case, polynomials $P_0$ and $P_1$ should be included to match the coordinates of the leading- (l.e.) and trailing-edges (t.e.) of the NACA 44xx airfoils. Figure 3a shows how the camber line of the NACA 44xx airfoils is approximated by the Legendre polynomials, whereas Fig. 3b compares the accuracy of these approximated camber lines using the piecewise relative errors. The polynomials starting from $P_2$ are called "flexible terms." It can be seen that 2–4 flexible terms are sufficient for the purpose of approximating the shape of the airfoil's camber line, resulting in piecewise errors less than 4% of the maximum camber. The modal assurance criterion (MAC) number and rms error of the approximated camber shapes compared with the exact camber line of NACA 44xx airfoils are listed in Table 1.

The aerodynamic lift and moment of the cambered thin airfoil is calculated by using Eqs. (21) and (22), with a variable pitching angle $\alpha$ on top of the camber shape. The aerodynamic lift and moment coefficients are

$$\begin{aligned} \alpha^0 &= \frac{\eta_1}{b} + \frac{3\eta_2}{2b} + \frac{9\eta_3}{4b} + \frac{45\eta_4}{16b} + \frac{225\eta_5}{64b} + \frac{945\eta_6}{512b} + \cdots \\ c_L &= 2\pi(\alpha - \alpha^0) \\ c_M &= -\pi\left(\frac{3\eta_2}{4b} + \frac{15\eta_3}{16b} + \frac{45\eta_4}{32b} + \frac{105\eta_5}{64b} + \frac{945\eta_6}{1024b} + \cdots\right) \end{aligned} \tag{32}$$

where $\alpha^0$ is the equivalent zero lift angle. The lift coefficients calculated using different numbers of flexible terms (Legendre polynomials) are plotted in Fig. 4a, whereas the moment coefficients are plotted in Fig. 4b. In general, the piecewise difference between the lift coefficients predicted using one flexible term and five flexible terms is about 0.05. Compared with the order of lift coefficient $c_L$ around one, this difference is reasonably small. The moment coefficient is also well converged by adding Legendre polynomials. Moreover, the zero lift angle can also be accurately predicted, as seen from Table 2. In this table, the zero lift angles predicted by the current formulation are compared with a family of NACA four-digit airfoils with the same camber but different thicknesses. The lift coefficients of these NACA airfoils calculated by using XFoil are plotted in Fig. 5, where the slopes of the curves reduce from 7.05 (for NACA 4415) to 6.51 (for NACA 4405). Obviously, the finite airfoil thickness makes the slopes of the lift curves deviate from $2\pi$. The current formulation does not take into account the airfoil thickness, which results in an exact slope of $2\pi$. Finally, it is important to point out that the current aerodynamic formulation with the camber degrees of freedom does not model the flow separation. Therefore, no stall effects are considered in the current study.

### B. Natural Modes and Frequencies of Flexible Airfoils

In this section, natural modes and frequencies of a uniform flexible airfoil are studied. The mass and bending rigidity properties are selected as $m = 40$ kg/m and $EI = 20$ N · m, respectively. The natural frequencies and mode shapes of the free–free airfoil can be obtained by solving the eigenvalue problem involving only the camber inertia $I_\eta$ and stiffness $K_\eta$, with neither the linear and torsional springs nor additional boundary conditions. Note that one

**Table 1 MAC number and rms error of approximated camber lines**

| Flexible terms | 1 | 2 | 3 | 4 | 5 |
|---|---|---|---|---|---|
| MAC number | $9.964 \times 10^{-1}$ | $9.998 \times 10^{-1}$ | $9.999 \times 10^{-1}$ | 1.000 | 1.000 |
| Rms error | $3.506 \times 10^{-3}$ | $9.052 \times 10^{-4}$ | $4.791 \times 10^{-4}$ | $3.378 \times 10^{-4}$ | $1.637 \times 10^{-4}$ |

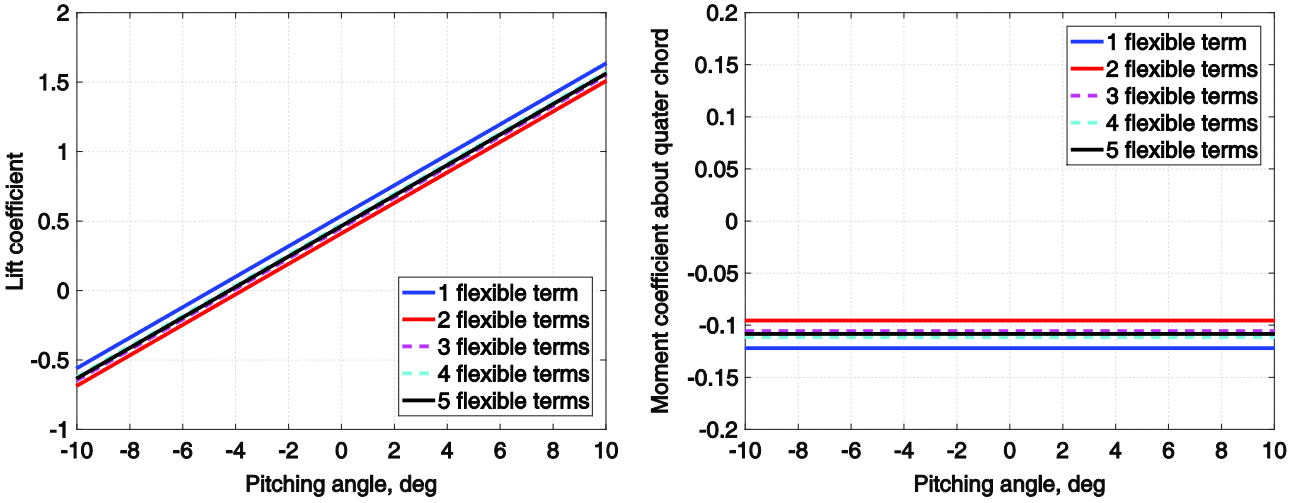


**a) Lift coefficient** **b) Moment coefficient about quarter chord**

**Fig. 4 Lift and moment coefficients of deformed flat airfoil.**

has to converge the eigenvalue solution by properly choosing polynomials $P_2$ and beyond, without using polynomials $P_0$ and $P_1$. On the other hand, as a uniform beam with a free–free boundary condition, the natural frequencies of the flexible airfoil may be obtained analytically:

$$\omega_i = (2k_i b)^2 \sqrt{\frac{EI}{8\ mb^3}} \tag{33}$$

where $k_i$ should satisfy the characteristic equation of a uniform free–free beam, such that

$$\cos(2k_i b)\cosh(2k_i b) = 1 \tag{34}$$

The two types of solutions of the natural frequencies of the flexible airfoil are compared and listed in Table 3. The mode shapes obtained using eight flexible terms are also compared with the analytical solution (Fig. 6). It can be seen that the approximate solution with only one flexible term ($P_2$) has an error of 20%. This is expected when solving the beam natural frequency using Rayleigh's quotient. The accuracy of the approximate solution is improved by adding more flexible terms, even though the higher-order modes are still not accurately calculated. For this uniform airfoil, its mode shapes are strictly either symmetric or antisymmetric. Therefore, adding antisymmetric polynomials (e.g., $P_3$, $P_5$, etc.) does not improve the accuracy of the symmetric modes (e.g., mode 1, mode 3, etc.). For the same reason, symmetric polynomials do not contribute to antisymmetric modes either. From the observation, it is sufficient to approximate the first two modes with relative errors of 0.85 and 3.02%, respectively, by using the first four flexible terms ($P_2$–$P_5$). However, to include more polynomials, even though providing accurate solutions of the higher-order modes, may significantly complicate the whole aeroelastic formulation shown in Eq. (24), especially the calculation of aerodynamic loads. Because the high-frequency modes usually do not have significant impacts on the overall dynamic response of the airfoil, one does not have to precisely capture these modes.

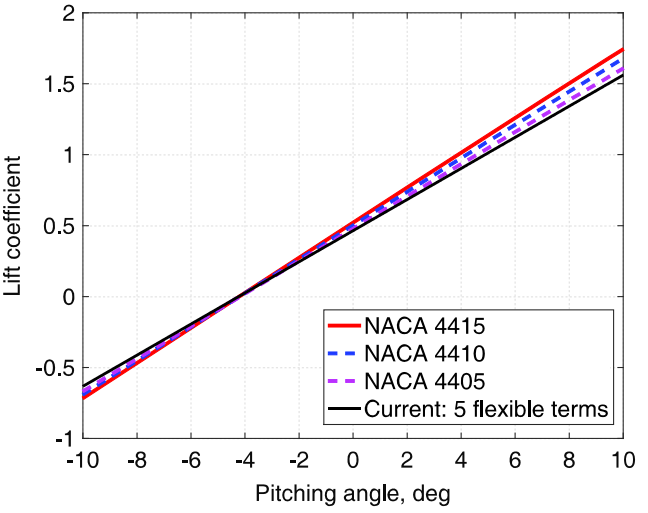


**Fig. 5 Lift coefficients of airfoils with same camber but different thicknesses.**

### C. Dimensionless Quantities

To facilitate the studies of static and dynamic aeroelastic characteristics of flexible airfoils with different combinations of properties, some variables are nondimensionalized. In static analyses, because the linear spring does not significantly impact the static instability of the airfoil, it is fixed as a constant, whereas the torsional spring constant and bending rigidity of the airfoil are both nondimensionalized using ratios against the linear spring constant. This allows for the variations of the rigidity properties of both the torsional spring and the airfoil. Above all, uniform thin, flat airfoils are studied with the location of the elastic axis represented as the dimensionless variable $a$. The airfoil is placed in a freestream, where the dynamic pressure is also scaled by the linear spring constant, such that $q = r_3 K_\xi$, while $r_3$ varies from zero until it reaches the critical divergence dynamic pressure. Additional dimensionless quantities in static analyses are listed in Table 4. In dynamic analyses, however, the current work follows the same convention in Bisplinghoff et al. [27]

**Table 2 Zero lift angles of deformed flat and NACA airfoils**

| | Deformed flat airfoil | | | | | NACA 4415 | NACA 4410 | NACA 4405 |
|---|---|---|---|---|---|---|---|---|
| Flexible terms | 1 | 2 | 3 | 4 | 5 | — — | — — | — — |
| Zero lift angle, deg | −4.90 | −3.75 | −4.12 | −4.35 | −4.23 | −4.22 | −4.21 | −4.18 |

**Table 3 Solutions of natural frequencies of the flexible airfoil[a]**

| Solution | Mode 1 | 2 | 3 | 4 | 5 | 6 |
|---|---|---|---|---|---|---|
| 1 flex term | 18.9736 | — — | — — | — — | — — | — — |
| 2 flex terms | 18.9736 | 64.8066 | — — | — — | — — | — — |
| 3 flex terms | 15.9553 | 64.8066 | 157.937 | — — | — — | — — |
| 4 flex terms | 15.9553 | 44.9275 | 157.937 | 322.197 | — — | — — |
| 5 flex terms | 15.8204 | 44.9275 | 91.3704 | 322.197 | 586.636 | — — |
| 6 flex terms | 15.8204 | 43.6200 | 91.3704 | 159.096 | 586.636 | 985.108 |
| 7 flex terms | 15.8203 | 43.6200 | 85.6344 | 159.096 | 253.653 | 985.108 |
| 8 flex terms | 15.8203 | 43.6091 | 85.6344 | 142.170 | 253.653 | 381.903 |
| Analytical | 15.8203 | 43.6093 | 85.4916 | 141.322 | 211.111 | 294.857 |

[a]Measurements are given in units of radians per second.

and Murua et al. [18], such that the nominal plunging–pitching frequency ratio $\omega_\xi/\omega_\alpha$ and the nominal bending–pitching frequency ratio $\omega_\eta/\omega_\alpha$ are used, as listed in Table 5. Note that the frequency ratio $\omega_\eta/\omega_\alpha$ is calculated by using analytical solution of the airfoil's first free bending frequency [see Eq. (33)]. In all cases, the pitching angle of the airfoil when the torsional spring is not stretched is set to $\alpha_0 = 2$ deg.

### D. Static Aeroelastic Behavior of Flexible Airfoils

In the static analysis, the two springs are attached at the midchord of the airfoil (e.g., $a = 0$), such that the gravitational force does not impact the pitching of the airfoil. To begin with, a stronger flexible airfoil is studied with the nondimensional rigidities being $r_1 = 1$ and $r_2 = 15$. From the previous studies, it has been learned that four flexible terms of the Legendre polynomials are suitable for most cases, capturing the first two bending modes of the airfoil and yielding sufficiently accurate aerodynamic load prediction with the camber. In the following studies, up to four Legendre polynomials are used to model the flexible deformation of the airfoil and the associated aerodynamic loads. The corresponding aerodynamic equations are listed in the Appendix. The resulting pitching angle $\alpha$ and the magnitude $\eta_2$ of polynomial $P_2$ are plotted in Fig. 7a with the change of the dynamic pressure. The same process is then repeated for a softer airfoil ($r_1 = 1$ and $r_2 = 1.5$) and the resulting $\alpha$ and $\eta_2$ are plotted in Fig. 7b. From the comparison of the two plots, it is evident that the flexibility of the airfoil does bring down the divergence dynamic pressure (from above 0.6 to less than 0.5). The stronger airfoil tends to gradually approach the critical pressure, as can be seen from Fig. 7a, no matter how many flexible terms are involved in the solution. Basically, the airfoil's camberwise flexibility does not significantly impact its static aeroelastic behavior. However, the softer airfoil may exhibit a sudden divergence, as can be observed from the solutions with 2–4 flexible terms in Fig. 7b. In these cases,

**Table 4 Dimensionless quantities in static aeroelastic analysis**

| Quantity | Variable | Dimensionless variable |
|---|---|---|
| Linear spring constant | $K_\xi$ | — — |
| Torsional spring constant | $K_\alpha$ | $r_1 = K_\alpha/(4b^2K_\xi)$ |
| Airfoil bending rigidity | $EI$ | $r_2 = EI/((1/18)b^3K_\xi)$ |
| Dynamic pressure | $q$ | $r_3 = q/K_\xi$ |
| Location of elastic axis | $d$ | $a = d/b$ |
| Plunging motion | $\xi$ | $\xi/b$ |
| Camber degrees of freedom | $\eta_i$ | $\eta_i/b$ |

**Table 5 Dimensionless quantities in dynamic aeroelastic analysis**

| Quantity | Variable | Dimensionless variable |
|---|---|---|
| Mass | $m$ | $m/\pi\rho b^2$ |
| Structural imbalance | $S_\alpha$ | $x_\alpha = S_\alpha/mb$ |
| Pitching moment of inertia | $I_\alpha$ | $r_\alpha = \sqrt{I_\alpha/mb^2}$ |
| Torsional spring constant | $K_\alpha$ | — — |
| Linear spring constant | $K_\xi$ | $\omega_\xi/\omega_\alpha = \sqrt{K_\xi/m}/\sqrt{K_\alpha/I_\alpha}$ |
| Airfoil bending rigidity | $EI$ | $\omega_\eta/\omega_\alpha = 4.73^2\sqrt{(EI)/(8mb^3)}/\sqrt{K_\alpha/I_\alpha}$ |
| Freestream velocity | $U_0$ | $U_0/\omega_\alpha b$ |
| Time | $t$ | $\omega_\alpha t/2\pi$ |

the aeroelastic system loses both the torsional rigidity and the bending rigidity of the airfoil, resulting in diverging solutions of both the pitching angle and the camber deformation. If only one flexible term is involved in the solution of the softer airfoil, the sudden torsional divergence is not observed. Instead, only the airfoil itself loses the bending rigidity and is folded together due to the aerodynamic force on it, whereas the pitching angle is still less than 10 deg. The solution simply stops without further increase of the dynamic pressure.

To further explore the impact of the airfoil flexibility on its static aeroelastic behavior, the dimensionless dynamic pressure $r_3$ is fixed at 0.4, whereas the airfoil bending rigidity is allowed to vary from 1.5 to 15. A sequence of static aeroelastic solutions are performed to identify the airfoil's static aeroelastic behavior with different levels of flexibility. A first check is performed by plotting the airfoil's pitching angle (Fig. 8a). It is of interest to see that adding the first flexible term $P_2$ does not change the pitching angle at all. This behavior is actually echoed in Fig. 7. Similarly, the third flexible term $P_4$ also seems to have no impact on the pitching angle. In reality, the two polynomials also make no contributions to the aerodynamic moment (Fig. 8b).

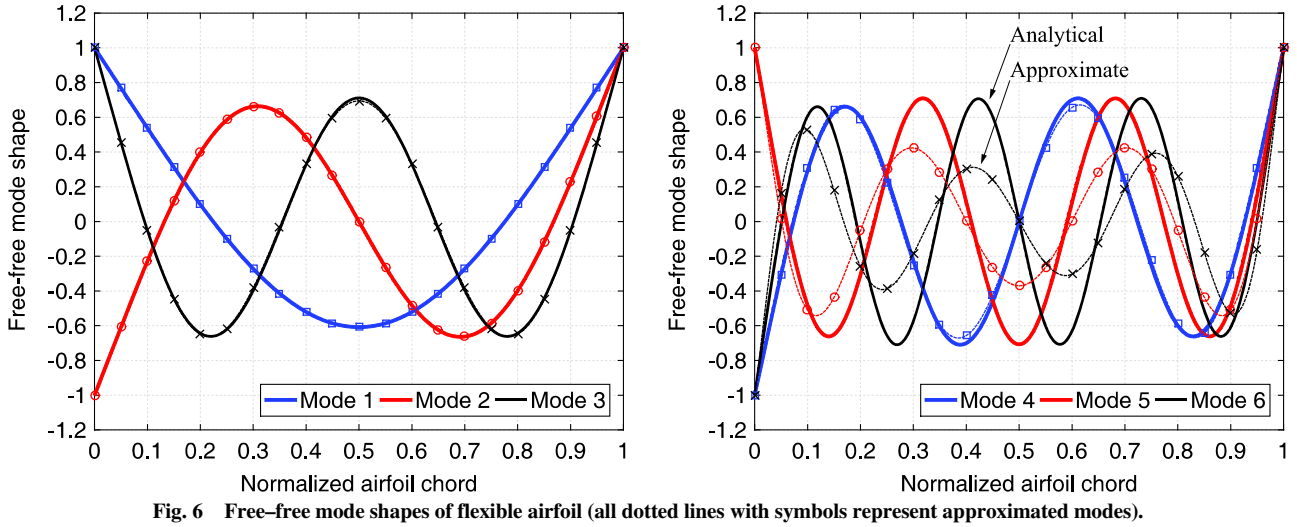


**Fig. 6 Free–free mode shapes of flexible airfoil (all dotted lines with symbols represent approximated modes).**

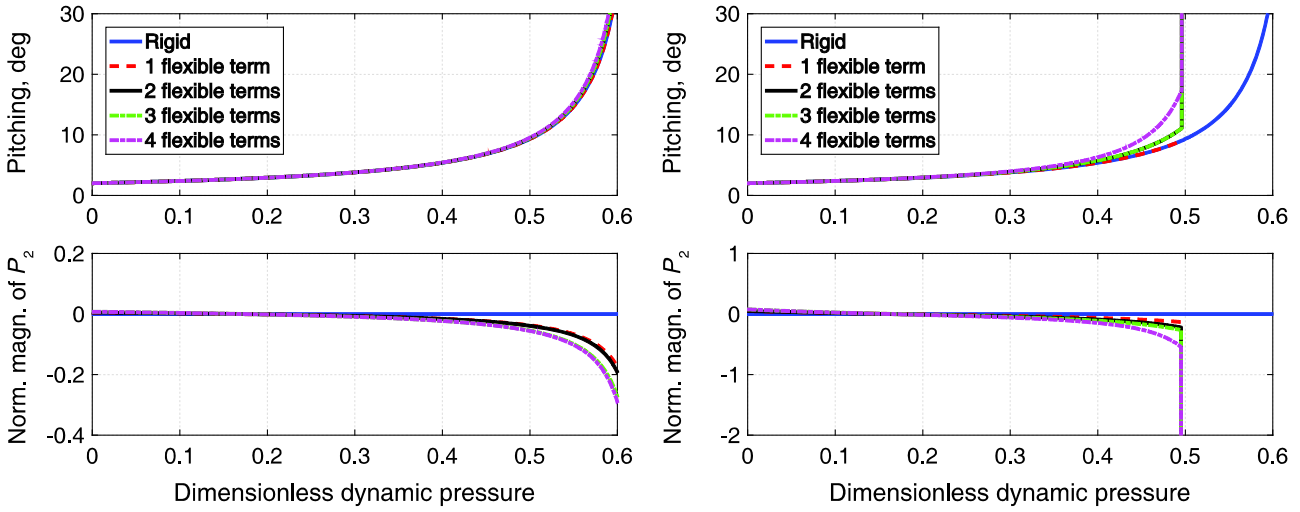


**a) Stronger airfoil $r_2 = 1.5$** **b) Softer airfoil $r_2 = 1.5$**

**Fig. 7 Pitching angles of two airfoils from solutions involving different numbers of flexible terms.**

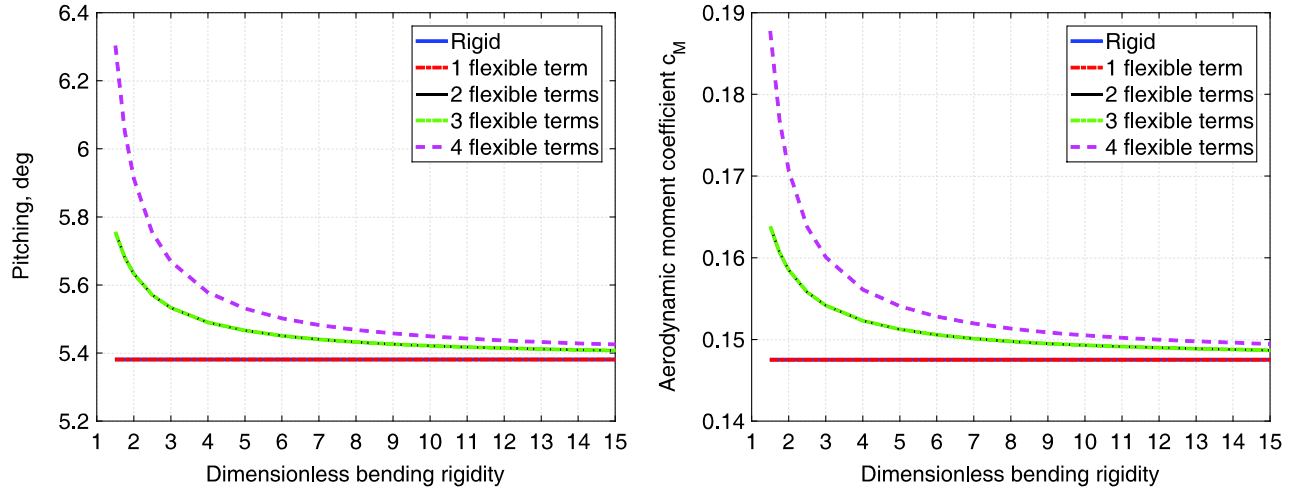


**a) Pitching angle** **b) Aerodynamic moment coefficient**

**Fig. 8 Pitching angle and aerodynamic moment coefficient of the airfoil with different levels of flexibility.**

This is simply because the elastic axis is placed at the midchord. A zero value of $a$ (thus, $d$) cancels the contributions of both $\eta_2$ and $\eta_4$ in Eq. (A3) in the Appendix. However, these magnitudes of polynomials still impact the solution of lift and thus the plunging motion (Fig. 9). If one further looks at the magnitudes of the Legendre polynomials, especially in the solution that involves the first four flexible terms (Fig. 10), it can be identified that the first polynomial is always the most significant when compared with the rest. However, with the reduction of the airfoil bending rigidity, the contributions of higher-order polynomials increase. Nonetheless, the dominant negative $\eta_2$ means the airfoil is mainly bent up, as seen from Fig. 11. The negative camber creates a negative equivalent angle of attack [Eq. (A8)] and thus the negative lift. When the airfoil is soft enough, this negative contribution may outperform the positive aerodynamic lift generated from the positive pitching angle. That is why the lift coefficient of the airfoil turns to be negative when the rigidity of the airfoil is below three (Fig. 9b). Note that the large bending deformation of the soft airfoils (e.g., $r_2 = 1.5$) in Fig. 11 may break the assumption of linear structural behavior in this study. However, the current development is still good for qualitative analysis of such airfoils. Regarding the impact of airfoil flexibility on its static aeroelastic behavior, it can be seen that an approximate solution using only one camber mode is not always accurate enough. A convergence study is needed to ensure the truncated modes (polynomials) are actually negligible for a given airfoil.

One more study is performed by moving the elastic axis to the quarter chord point from the leading edge ($a = -0.5$). The airfoil should be always statically stable and no divergence speed can be found if it is rigid. However, the camberwise flexibility of the airfoil may change this property. Figure 12 demonstrates the variation of the divergence dynamic pressure with the airfoil rigidity, where four solutions are carried out by using different numbers of Legendre polynomials. Obviously, the solution with only one polynomial can still capture the trend. However, one has to use at least three polynomials to reach enough accuracy.

### E. Flutter of Flexible Airfoils

The flutter speed of a rigid, thin plate airfoil with no camber flexibility is first calculated using the approach described in Sec. III. D, with no added structural damping in this calculation. As a validation of the flutter analysis approach, the current results are compared with those presented in [18,28,29]. The airfoil's elastic axis is located at $a = -0.3$, with a density ratio $m/\pi\rho b^2 = 20$ and dimensionless radius of gyration $r_\alpha^2 = 0.25$. The nominal plunging–pitching frequency ratio $\omega_\xi/\omega_\alpha$ varies from zero to two. The flutter boundary is also impacted by the location of the airfoil's c.g. $x_\alpha$ measured from its elastic axis. Figure 13 plots the dimensionless flutter speed with four different c.g. locations. Zeiler [29] identified that several results presented by Theodorsen and Garrick [28] were

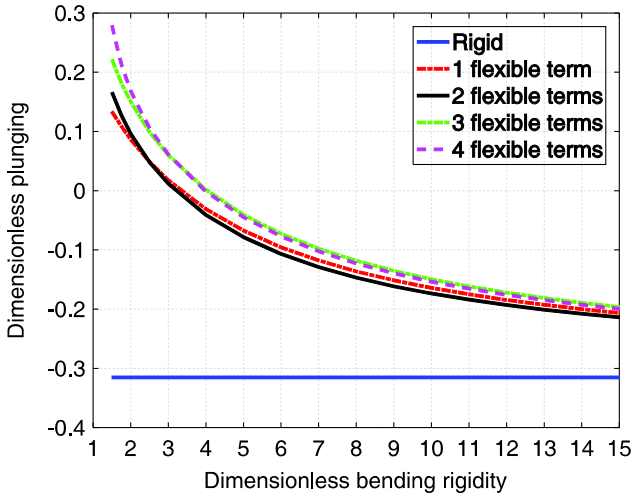


a) Plunging (positive down)

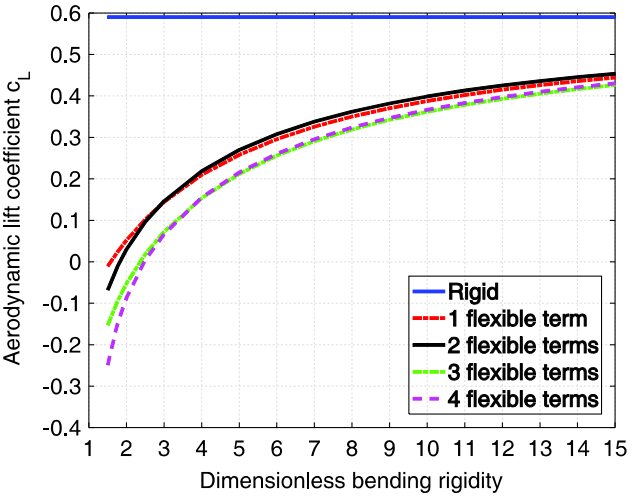


b) Aerodynamic lift coefficient

**Fig. 9 Plunging and aerodynamic lift coefficient of the airfoil with different levels of flexibility.**



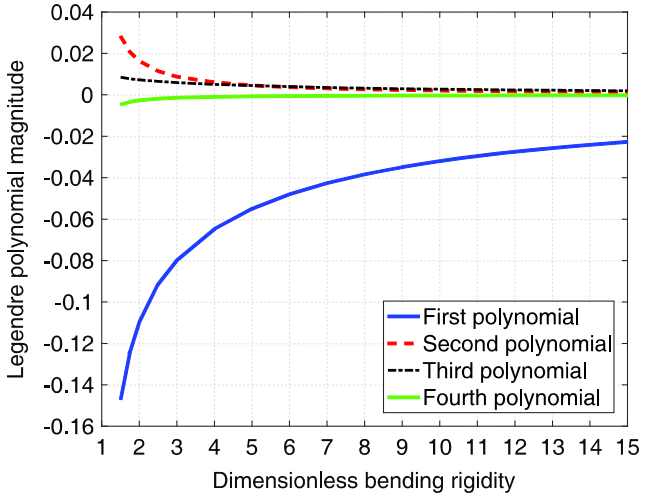


**Fig. 10 Normalized (about *b*) magnitudes of Legendre polynomials in the solution using four flexible terms.**

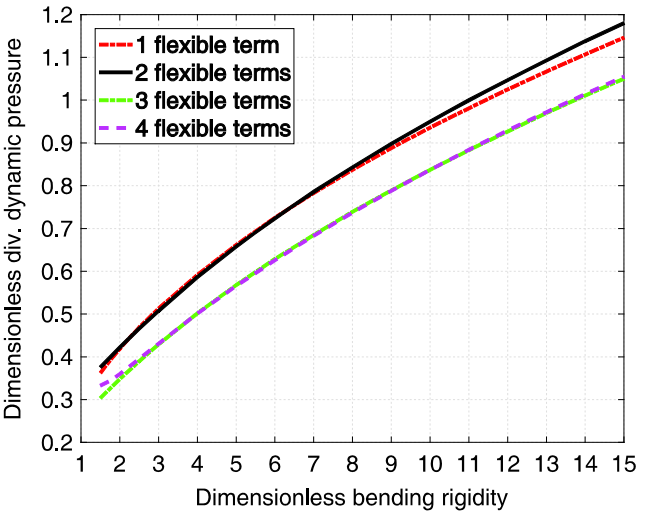


**Fig. 12 Static aerodynamic loads of the flexible airfoil.**

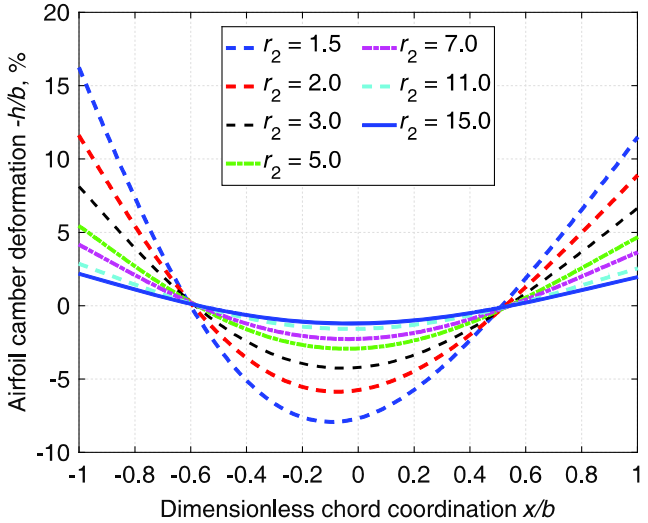


**Fig. 11 Airfoil camber deformations (percentage of semichord length) with different levels of flexibility.**

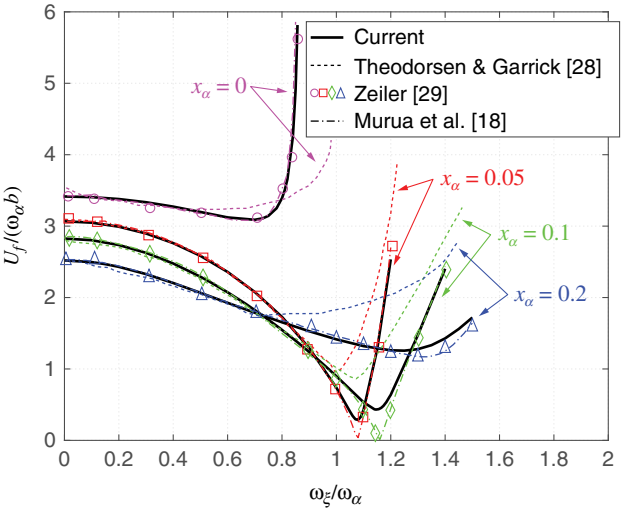


**Fig. 13 Comparison of flutter speed of a rigid airfoil from different solutions.**

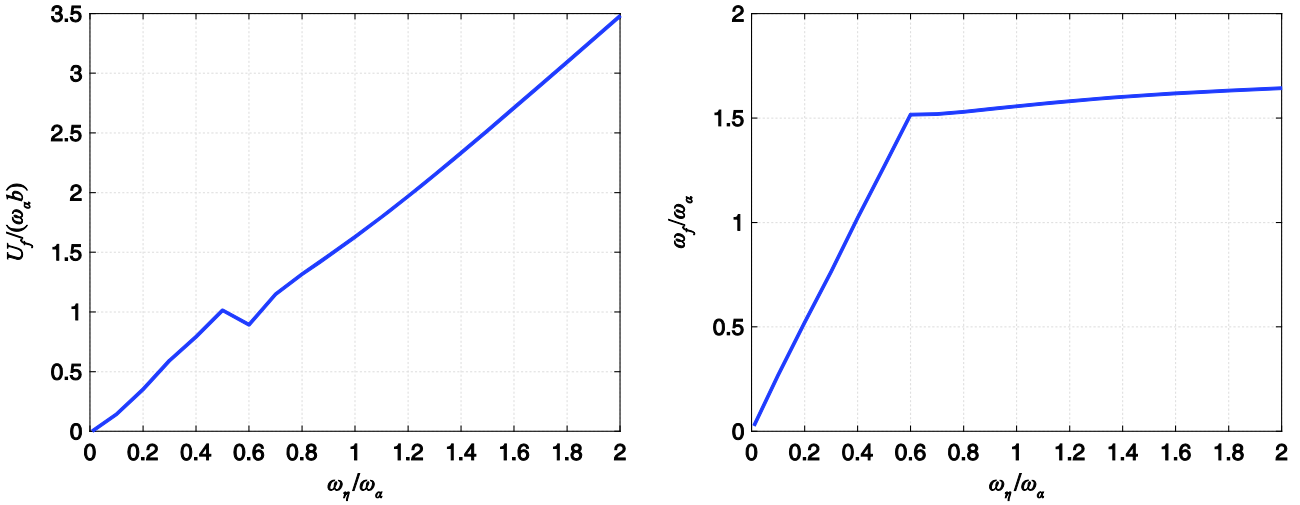


**a) Flutter speed** **b) Flutter frequency**

**Fig. 14 Flutter speed of the flexible airfoil.**

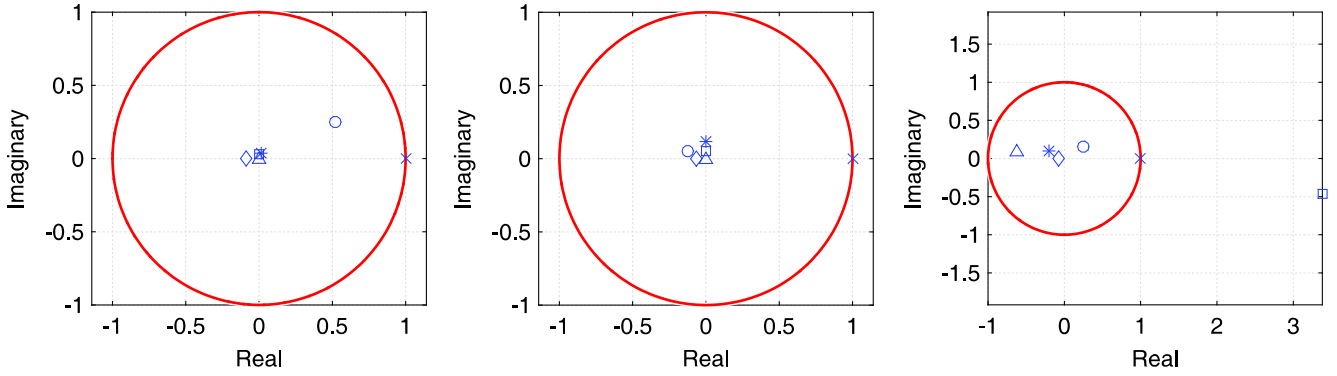


**a) $\omega_\eta/\omega_\alpha = 2$** **b) $\omega_\eta/\omega_\alpha = 1$** **c) $\omega_\eta/\omega_\alpha = 0.5$**

**Fig. 15 Vector diagram of unstable modes, normalized by the magnitude of the first camber degree of freedom.**

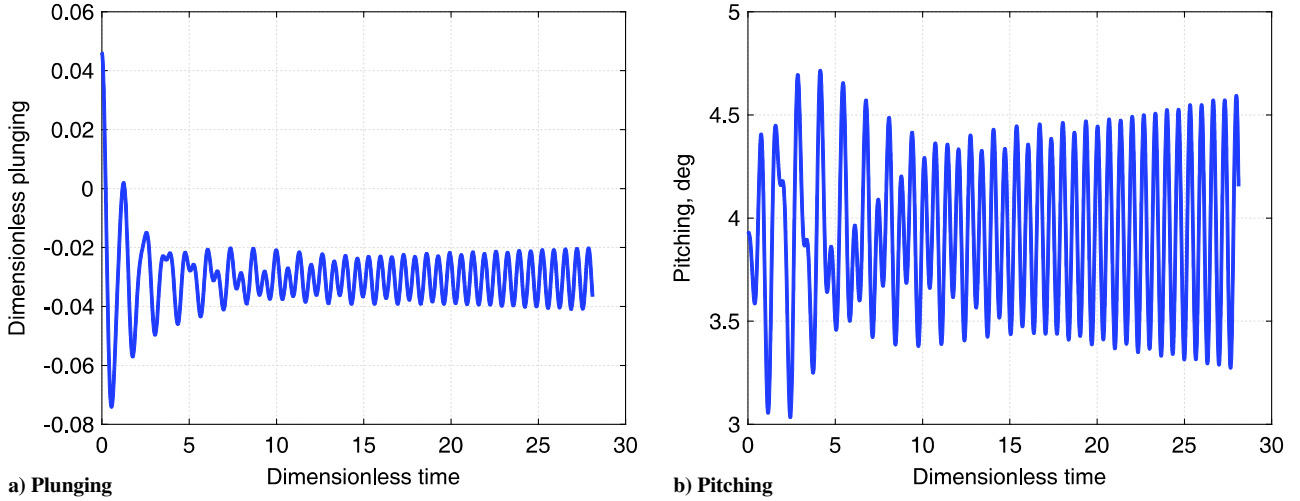


**a) Plunging** **b) Pitching**

**Fig. 16 Rigid-body motions of postflutter case ($U_0 = 1.1U_f$, $\omega_\eta/\omega_\alpha = 1$, and $\omega_\xi/\omega_\alpha = 1$).**

not accurate. Except for missing the extreme values around $\omega_\xi/\omega_\alpha = 1.15$ for $x_\alpha = 0.1$, the current results match perfectly with [18,29], both of which used a $V$–$g$ method for the flutter calculation. Note that Bisplinghoff et al. [27] also did not report the deep valleys of the data in the same frequency ratio range.

The previous case does not include the camber deformation of the airfoil. For a better study of the impact on airfoil's flexibility on the flutter boundary, a uniform thin, flat airfoil is studied with the following dimensionless properties: $m/\pi\rho b^2 = 20$, $a = 0$, $x_\alpha = 0$, and $r_\alpha^2 = 1/3$. The nominal frequency ratio $\omega_\xi/\omega_\alpha$ is kept as one, whereas $\omega_\eta/\omega_\alpha$ is allowed to vary. To eliminate unrealistic impact from the high-frequency camber modes and to remove the impact of some neutrally stable root loci, a stiffness-proportional damping with a damping coefficient of 0.001 is added to the equation of motion. Four Legendre polynomials ($P_2$–$P_5$) are included in the flutter calculations. The obtained

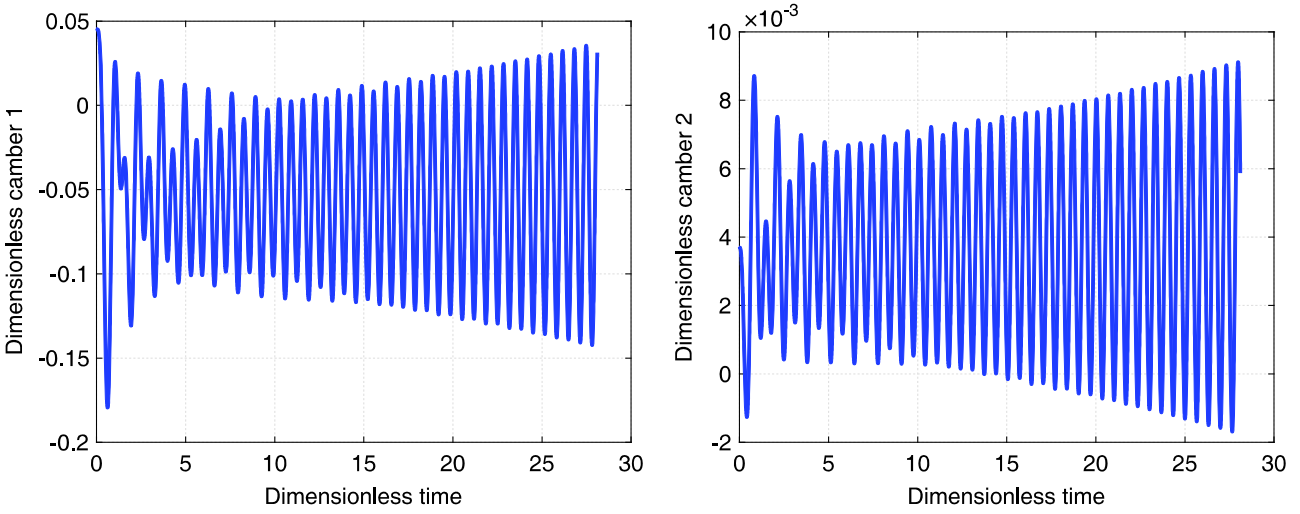


a) First camber dof: $\eta_2$ b) Second camber dof: $\eta_3$

**Fig. 17 First two camber degrees of freedom of postflutter case ($U_0 = 1.1U_f$, $\omega_\eta/\omega_\alpha = 1$, and $\omega_\xi/\omega_\alpha = 1$).**

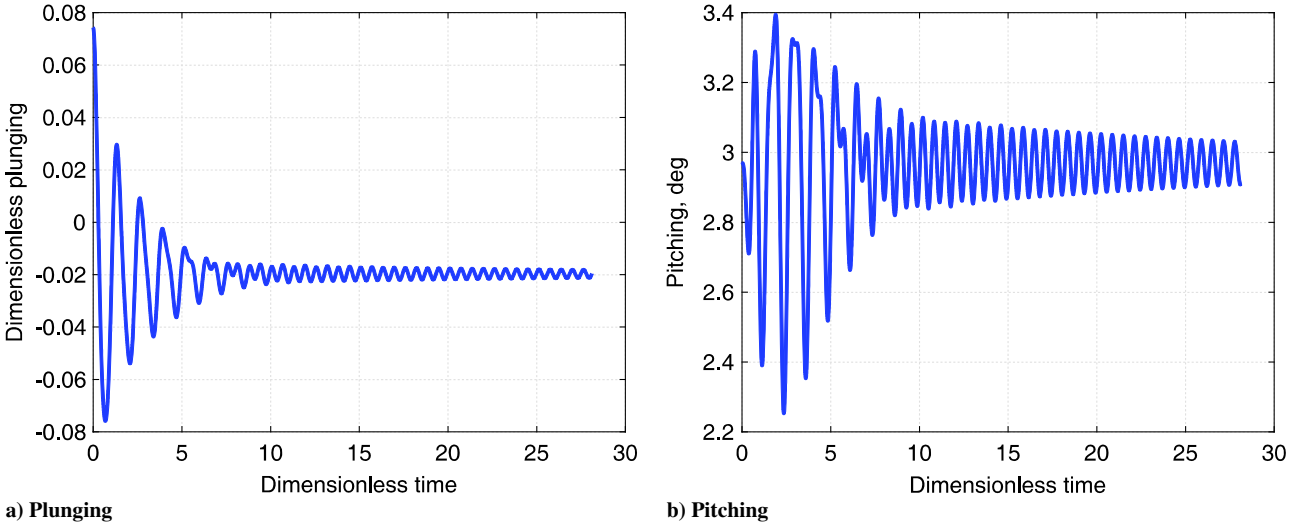


a) Plunging b) Pitching

**Fig. 18 Rigid-body motions of preflutter case ($U_0 = 0.9U_f$, $\omega_\eta/\omega_\alpha = 1$, and $\omega_\xi/\omega_\alpha = 1$).**

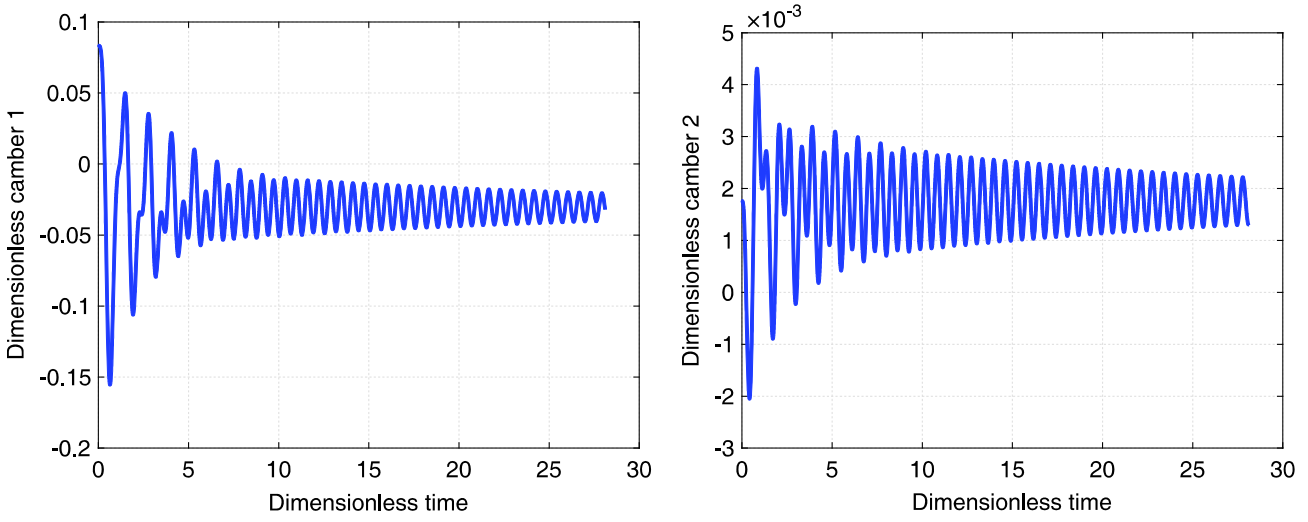


a) First camber dof: $\eta_2$ b) Second camber dof: $\eta_3$

**Fig. 19 First two camber degrees of freedom of preflutter case ($U_0 = 0.9U_f$, $\omega_\eta/\omega_\alpha = 1$, and $\omega_\xi/\omega_\alpha = 1$).**

flutter speeds with the change of $\omega_\eta/\omega_\alpha$ are then plotted in Fig. 14a. When the airfoil bending rigidity is higher than 0.6, the flutter is dominated by the first camber degree of freedom (DOF), as can be observed from the diagram of the unstable mode (Fig. 15a), even though the coupling with the plunging degree may change (Fig. 15b) when the airfoil flexibility varies. Nonetheless, the change of mode shape is gradual and results in a smooth deduction of the flutter speed. However, if the airfoil gets more flexible, the driving component of instability shifts from the first to the second camber degree of freedom (Fig. 15c). The shift of mode shape also causes the flutter speed and frequency changes (Fig. 14) when $\omega_\eta/\omega_\alpha$ is between 0.5 and 0.6. It is also of interest to note that Murua et al. [18] also analyzed the flutter characteristics of the same airfoil. However, only one camber mode was included in their study and the airfoil's camber rigidity was obtained from a different approach. In addition, the structural damping is treated differently in the two studies. These have caused some disagreement between the current results and those from [18].

As a verification of the current flutter analysis results, a transient simulation is carried out with a freestream velocity of 1.1 times $U_f$, where the nominal frequency ratio $\omega_\eta/\omega_\alpha$ is fixed at 1.0. Figures 16 and 17 clearly show the instability of the rigid-body and flexible degrees of the aeroelastic system, which is otherwise stable if the freestream velocity is 0.9 times $U_f$ (see Figs. 18 and 19).

## IV. Conclusions

This paper aimed at providing an efficient solution to aeroelastic problems of flexible airfoils that were allowed to have arbitrary camber deformations in addition to rigid-body plunging and pitching motions. The orthogonal Legendre polynomials, defined along the airfoil chordwise length, were applied to represent arbitrary camber deformations of flexible airfoils. The solution's accuracy can be guaranteed by involving sufficient Legendre polynomials in the solution. With the arbitrary camber deformations represented by the combination of Legendre polynomials, the structural dynamic governing equations of flexible airfoils were derived by following Hamilton's principle. The unsteady aerodynamic loads, including the lift, moment, and associated camber loads, were obtained by extending the finite-state inflow theory, where the airfoil camber deformations that had been represented by the Legendre polynomials were further expanded using the Glauert expansion. The modified aerodynamic formulation may provide the required aerodynamic loads of thin airfoils with arbitrary rigid-body motions and camber deformations. The resulting aeroelastic system still remains of low order, where the series of Legendre polynomials can be truncated for approximate solutions, which is in nature more efficient than CFD or other panel methods.

The developed formulation was then tested in different aspects. First, the analytical camber line of a standard cambered NACA four-digit airfoil was approximated by using the expansion of the Legendre polynomials. As expected, by selecting a sufficient number of Legendre polynomials, the airfoil camber was very accurately represented by these polynomials. The static aerodynamic loads on the approximated airfoil were also compared with the loads of NACA four-digit airfoils calculated using XFoil. It was verified that the current aerodynamic formulation could perfectly model the loads on thin airfoils, yet further corrections (e.g., using the conformal mapping of the airfoil contour) would be required to model airfoils with finite thickness. In addition, the current aerodynamic formulation only considered inviscid and incompressible flow. No stall effects were considered in the formulation.

Finally, the static and dynamic aeroelastic characteristics of a flexible airfoil were explored. The camber flexibility did bring down the critical divergence pressure. It is well known that an airfoil should not diverge if its elastic axis is located at or in front of the aerodynamic center. However, this will break if the camberwise flexibility is considered. The torsional divergence was obviously observed if the airfoil turned to be flexible. In addition, the flutter boundary of the airfoil was also significantly reduced if the airfoil's flexibility was considered in the modeling. Especially, the dominant unstable degree shifted between the first two camber degrees of freedom, if the flexibility of the airfoil varied. After all, from this study, it can be concluded that wing camberwise flexibility should be properly considered in designs and studies of morphing wings or membrane wings, where either the structural or aerodynamic camber shape can change in the operation. The newly introduced camberwise flexibility may significantly alter the aeroelastic behavior of the system.

## Appendix: 2-D Unsteady Aerodynamic Loads with Legendre Polynomials $P_2$–$P_5$

Aerodynamic loads acting on a flexible airfoil are calculated using four Legendre polynomials ($P_2$–$P_5$) to represent the airfoil's camber deformation. The generalized aerodynamic loads are

$$
\begin{aligned}
\mathcal{L}_0 &= -\pi\rho b^2\left(\ddot{\xi}+U_0\dot{\alpha}-d\ddot{\alpha}-\frac{1}{8}\ddot{\eta}_2-\frac{1}{64}\ddot{\eta}_4\right)\\
&\quad -2\pi\rho bU_0^2\left[\alpha+\frac{\dot{\xi}}{U_0}+\left(\frac{1}{2}b-d\right)\frac{\dot{\alpha}}{U_0}-\frac{\lambda_0}{U_0}\right]\\
&\quad -2\pi\rho bU_0^2\left(\frac{3}{2}\frac{\eta_2}{b}+\frac{9}{4}\frac{\eta_3}{b}+\frac{45}{16}\frac{\eta_4}{b}+\frac{225}{64}\frac{\eta_5}{b}+\frac{1}{4}\frac{\dot{\eta}_2}{U_0}+\frac{3}{8}\frac{\dot{\eta}_3}{U_0}\right.\\
&\quad \left.+\frac{9}{64}\frac{\dot{\eta}_4}{U_0}+\frac{15}{64}\frac{\dot{\eta}_5}{U_0}\right)\\
\mathcal{L}_1 &= -\pi\rho b^2\left(\frac{1}{8}b\ddot{\alpha}-\frac{1}{32}\ddot{\eta}_3-\frac{5}{1024}\ddot{\eta}_5\right)\\
&\quad -2\pi\rho bU_0^2\left(-\frac{1}{2}\alpha-\frac{1}{2}\frac{\dot{\xi}}{U_0}+\frac{1}{2}d\frac{\dot{\alpha}}{U_0}+\frac{1}{2}\frac{\lambda_0}{U_0}\right)\\
&\quad -2\pi\rho bU_0^2\left(-\frac{3}{16}\frac{\eta_3}{b}-\frac{15}{128}\frac{\eta_5}{b}+\frac{1}{4}\frac{\dot{\eta}_2}{U_0}+\frac{11}{128}\frac{\dot{\eta}_4}{U_0}\right)\\
\mathcal{L}_2 &= -\pi\rho b^2\left(-\frac{1}{2}\ddot{\xi}-U_0\dot{\alpha}+\frac{1}{2}d\ddot{\alpha}+\frac{1}{8}\ddot{\eta}_2-\frac{3}{256}\ddot{\eta}_4\right)\\
&\quad -2\pi\rho bU_0^2\left(-\frac{3}{4}\frac{\eta_2}{b}-\frac{5}{16}\frac{\eta_4}{b}+\frac{1}{8}\frac{\dot{\eta}_3}{U_0}+\frac{5}{256}\frac{\dot{\eta}_5}{U_0}\right)\\
\mathcal{L}_3 &= -\pi\rho b^2\left(-\frac{1}{8}b\ddot{\alpha}+\frac{9}{128}\ddot{\eta}_3-\frac{9}{1024}\ddot{\eta}_5\right)\\
&\quad -2\pi\rho bU_0^2\left(-\frac{15}{16}\frac{\eta_3}{b}-\frac{105}{256}\frac{\eta_5}{b}-\frac{3}{8}\frac{\dot{\eta}_2}{U_0}+\frac{15}{128}\frac{\dot{\eta}_4}{U_0}\right)\\
\mathcal{L}_4 &= -\pi\rho b^2\left(-\frac{1}{16}\ddot{\eta}_2+\frac{3}{64}\ddot{\eta}_4\right)-2\pi\rho bU_0^2\left(-\frac{35}{32}\frac{\eta_4}{b}-\frac{5}{16}\frac{\dot{\eta}_3}{U_0^2}+\frac{7}{64}\frac{\dot{\eta}_5}{U_0}\right)\\
\mathcal{L}_5 &= -\pi\rho b^2\left(-\frac{5}{128}\ddot{\eta}_3+\frac{35}{1024}\ddot{\eta}_5\right)\\
&\quad -2\pi\rho bU_0^2\left(-\frac{315}{256}\frac{\eta_5}{b}-\frac{35}{128}\frac{\dot{\eta}_4}{U_0}\right)
\end{aligned}
\tag{A1}
$$

where $\eta_2$–$\eta_5$ are the magnitudes of Legendre polynomials $P_2$–$P_5$, respectively. By following Eqs. (22) and (23), all resultant aerodynamic loads can be calculated based on the generalized loads, for example, the aerodynamic lift, moment, and first four camber loads are

$$
\begin{aligned}
\mathcal{L} &= \pi\rho b^2(\ddot{\xi}+U_0\dot{\alpha}-d\ddot{\alpha})\\
&\quad +2\pi\rho bU_0^2\left[\alpha+\frac{\dot{\xi}}{U_0}+\left(\frac{1}{2}b-d\right)\frac{\dot{\alpha}}{U_0}-\frac{\lambda_0}{U_0}\right]\\
&\quad -\pi\rho b^2\left(-\frac{1}{8}\ddot{\eta}_2-\frac{1}{64}\ddot{\eta}_4\right)\\
&\quad +2\pi\rho bU_0^2\left(\frac{3}{2}\frac{\eta_2}{b}+\frac{9}{4}\frac{\eta_3}{b}+\frac{45}{16}\frac{\eta_4}{b}+\frac{225}{64}\frac{\eta_5}{b}+\frac{1}{4}\frac{\dot{\eta}_2}{U_0}+\frac{3}{8}\frac{\dot{\eta}_3}{U_0}\right.\\
&\quad \left.+\frac{9}{64}\frac{\dot{\eta}_4}{U_0}+\frac{15}{64}\frac{\dot{\eta}_5}{U_0}\right)
\end{aligned}
\tag{A2}
$$

$$\mathcal{M} = \pi\rho b^2\left[d\ddot{\xi} - \left(\frac{1}{2}b - d\right)U_0\dot{\alpha} - \left(\frac{1}{8}b^2 + d^2\right)\ddot{\alpha}\right] + 2\pi\rho b U_0^2\left(\frac{1}{2}b + d\right)\left[\alpha + \frac{\dot{\xi}}{U_0} + \left(\frac{1}{2}b - d\right)\frac{\dot{\alpha}}{U_0} - \frac{\lambda_0}{U_0}\right] + \pi\rho b^2\left(-\frac{1}{8}d\ddot{\eta}_2 + \frac{1}{32}b\ddot{\eta}_3 - \frac{1}{64}d\ddot{\eta}_4 + \frac{5}{1024}b\ddot{\eta}_5\right) + 2\pi\rho b U_0^2\left[\left(\frac{3}{2}d\right)\frac{\eta_2}{b} + \left(\frac{3}{16}b + \frac{9}{4}d\right)\frac{\eta_3}{b} + \left(\frac{45}{16}d\right)\frac{\eta_4}{b} + \left(\frac{15}{128}b + \frac{225}{64}d\right)\frac{\eta_5}{b}\right] + 2\pi\rho b U_0^2\left[\left(-\frac{1}{4}b + \frac{1}{4}d\right)\frac{\dot{\eta}_2}{U_0} + \left(\frac{3}{8}d\right)\frac{\dot{\eta}_3}{U_0} + \left(-\frac{11}{128}b + \frac{9}{64}d\right)\frac{\dot{\eta}_4}{U_0} + \left(\frac{15}{64}d\right)\frac{\dot{\eta}_5}{U_0}\right] \tag{A3}$$

$$\mathcal{N}_1 = \pi\rho b^2\left(\frac{1}{8}\ddot{\xi} + \frac{1}{2}U_0\dot{\alpha} - \frac{1}{8}d\ddot{\alpha}\right) + \pi\rho b U_0^2\left[-\frac{1}{2}\alpha - \frac{1}{2}\frac{\dot{\xi}}{U_0} - \frac{1}{2}\left(\frac{1}{2}b - d\right)\frac{\dot{\alpha}}{U_0} + \frac{1}{2}\frac{\lambda_0}{U_0}\right] + \pi\rho b^2\left(-\frac{1}{16}\ddot{\eta}_2 + \frac{13}{1024}\ddot{\eta}_4\right) + \pi\rho b U_0^2\left(\frac{3}{8}\frac{\eta_2}{b} - \frac{9}{8}\frac{\eta_3}{b} - \frac{15}{16}\frac{\eta_4}{b} - \frac{450}{256}\frac{\eta_5}{b} - \frac{1}{8}\frac{\dot{\eta}_2}{U_0} - \frac{3}{8}\frac{\dot{\eta}_3}{U_0} - \frac{9}{128}\frac{\dot{\eta}_4}{U_0} - \frac{75}{512}\frac{\dot{\eta}_5}{U_0}\right) \tag{A4}$$

$$\mathcal{N}_2 = \pi\rho b^2\left(\frac{1}{32}b\ddot{\alpha}\right) + \pi\rho b U_0^2\left(\frac{3}{8}\alpha + \frac{3}{8}\frac{\dot{\xi}}{U_0} - \frac{3}{8}d\frac{\dot{\alpha}}{U_0} - \frac{3}{8}\frac{\lambda_0}{U_0}\right) + \pi\rho b^2\left(-\frac{33}{1024}\ddot{\eta}_3 + \frac{15}{1024}\ddot{\eta}_5\right) + \pi\rho b U_0^2\left(\frac{21}{16}\frac{\eta_3}{b} + \frac{615}{1024}\frac{\eta_5}{b} + \frac{9}{32}\frac{\dot{\eta}_2}{U_0} - \frac{27}{128}\frac{\dot{\eta}_4}{U_0}\right) \tag{A5}$$

$$\mathcal{N}_3 = \pi\rho b^2\left(\frac{1}{64}\ddot{\xi} + \frac{11}{64}U_0\dot{\alpha} - \frac{1}{64}d\ddot{\alpha}\right) + \pi\rho b U_0^2\left[-\frac{9}{32}\alpha - \frac{9}{32}\frac{\dot{\xi}}{U_0} - \frac{9}{32}\left(\frac{1}{2}b - d\right)\frac{\dot{\alpha}}{U_0} + \frac{9}{32}\frac{\lambda_0}{U_0}\right] + \pi\rho b^2\left(\frac{13}{1024}\ddot{\eta}_2 - \frac{81}{4096}\ddot{\eta}_4\right) + \pi\rho b U_0^2\left(\frac{3}{64}\frac{\eta_2}{b} - \frac{81}{128}\frac{\eta_3}{b} + \frac{615}{1024}\frac{\eta_4}{b} - \frac{2025}{2048}\frac{\eta_5}{b} - \frac{18}{256}\frac{\dot{\eta}_2}{U_0} + \frac{81}{512}\frac{\dot{\eta}_3}{U_0} - \frac{81}{2048}\frac{\dot{\eta}_4}{U_0} - \frac{405}{2048}\frac{\dot{\eta}_5}{U_0}\right) \tag{A6}$$

$$\mathcal{N}_4 = \pi\rho b^2\left(\frac{5}{1024}b\ddot{\alpha}\right) + \pi\rho b U_0^2\left(\frac{15}{64}\alpha + \frac{15}{64}\frac{\dot{\xi}}{U_0} - \frac{15}{64}d\frac{\dot{\alpha}}{U_0} - \frac{15}{64}\frac{\lambda_0}{U_0}\right) + \pi\rho b^2\left(\frac{15}{2048}\ddot{\eta}_3 - \frac{435}{32768}\ddot{\eta}_5\right) + \pi\rho b U_0^2\left(\frac{615}{1024}\frac{\eta_3}{b} + \frac{6105}{4096}\frac{\eta_5}{b} + \frac{45}{512}\frac{\dot{\eta}_2}{U_0} + \frac{675}{4096}\frac{\dot{\eta}_4}{U_0}\right) \tag{A7}$$

where the effective angle of attack is

$$\alpha_{\text{eff}} = \alpha + \frac{\dot{\xi}}{U_0} + \left(\frac{1}{2}b - d\right)\frac{\dot{\alpha}}{U_0} - \frac{\lambda_0}{U_0} + \frac{3}{2}\frac{\eta_2}{b} + \frac{9}{4}\frac{\eta_3}{b} + \frac{45}{16}\frac{\eta_4}{b} + \frac{225}{64}\frac{\eta_5}{b} + \frac{1}{4}\frac{\dot{\eta}_2}{U_0} + \frac{3}{8}\frac{\dot{\eta}_3}{U_0} + \frac{9}{64}\frac{\dot{\eta}_4}{U_0} + \frac{15}{64}\frac{\dot{\eta}_5}{U_0} \tag{A8}$$

## Acknowledgments

This work was partially supported by the NASA Ames Research Center under contract NNX15AG65G, with Sean S.-M. Swei as the Technical Monitor. The author also appreciates Cecilia K. King (formerly a graduate student of University of Alabama, now employed by NASA Marshall Space Flight Center) for generating some of the numerical results in the study.

## References

[1] Stanewsky, E., "Aerodynamic Benefits of Adaptive Wing Technology," *Aerospace Science and Technology*, Vol. 4, No. 7, 2000, pp. 439–452. doi:10.1016/S1270-9638(00)01069-5

[2] Hetrick, J., Osborn, R., Kota, S., Flick, P., and Paul, D., "Flight Testing of Mission Adaptive Compliant Wing," *48th AIAA/ASME/ASCE/AHS/ASC Structures, Structural Dynamics, and Materials Conference*, AIAA Paper 2007-1709, April 2007.

[3] Kota, S., Osborn, R., Ervin, G., Maric, D., Flick, P., and Paul, D., "Mission Adaptive Compliant Wing—Design, Fabrication and Flight Test," *RTO Applied Vehicle Technology Panel (AVT) Symposium*, NATO RTO-MP-AVT-168, April 2009.

[4] Bilgen, O., Kochersberger, K. B., Inman, D. J., and Ohanian, O. J., "Novel, Bidirectional, Variable-Camber Airfoil via Macro-Fiber Composite Actuators," *Journal of Aircraft*, Vol. 47, No. 1, 2010, pp. 303–314. doi:10.2514/1.45452

[5] Gandhi, F., Frecker, M., and Nissly, A., "Design Optimization of a Controllable Camber Rotor Airfoil," *AIAA Journal*, Vol. 46, No. 1, 2008, pp. 142–153. doi:10.2514/1.24476

[6] Kaul, U. K., and Nguyen, N. T., "Drag Optimization Study of Variable Camber Continuous Trailing Edge Flap (VCCTEF) Using OVERFLOW," *32nd AIAA Applied Aerodynamics Conference*, AIAA Paper 2014-2444, June 2014.

[7] Nguyen, N. T., and Ting, E., "Flutter Analysis of Mission-Adaptive Wing with Variable Camber Continuous Trailing Edge Flap," *55th AIAA/ASME/ASCE/AHS/ASC Structures, Structural Dynamics, and Materials Conference*, AIAA Paper 2014-0839, Jan. 2014.

[8] Null, W., and Shkarayev, S., "Effect of Camber on the Aerodynamics of Adaptive-Wing Micro Air Vehicles," *Journal of Aircraft*, Vol. 42, No. 6, 2005, pp. 1537–1542. doi:10.2514/1.12401

[9] Grishanina, T. V., and Shklyarchuk, F. N., "Unsteady Oscillation of a Deformable Airfoil Section in Incompressible Flow," *Russian Aeronautics*, Vol. 52, No. 2, 2009, pp. 129–137. doi:10.3103/S1068799809020019

[10] Guerrero, J. E., "Aerodynamic Performance of Cambered Heaving Airfoils," *AIAA Journal*, Vol. 48, No. 11, 2010, pp. 2694–2698. doi:10.2514/1.J050036

[11] Tay, W. B., and Lim, K. B., "Numerical Analysis of Active Chordwise Flexibility on the Performance of Non-Symmetrical Flapping Airfoils," *Journal of Fluids and Structures*, Vol. 26, No. 1, 2010, pp. 74–91. doi:10.1016/j.jfluidstructs.2009.10.005

[12] Swanson, T., and Isaac, K. M., "Planform and Camber Effects on the Aerodynamics of Low-Reynolds-Number Wings," *Journal of Aircraft*, Vol. 47, No. 2, 2010, pp. 613–621. doi:10.2514/1.45921

[13] Stanford, B. K., and Beran, P. S., "Analytical Sensitivity Analysis of an Unsteady Vortex-Lattice Method for Flapping-Wing Optimization," *Journal of Aircraft*, Vol. 47, No. 2, 2010, pp. 647–662. doi:10.2514/1.46259

[14] Murua, J., Palacios, R., and Graham, J. M. R., "Applications of the Unsteady Vortex-Lattice Method in Aircraft Aeroelasticity and Flight Dynamics," *Progress in Aerospace Sciences*, Vol. 55, Nov. 2012, pp. 46–72. doi:10.1016/j.paerosci.2012.06.001

[15] Joo, J. J., Marks, C. R., Zientarski, L., and Culler, A. J., "Variable Camber Compliant Wing—Design," *23rd AIAA/AHS Adaptive Structures Conference*, AIAA Paper 2015-1050, Jan. 2015.

[16] Miller, S. C., Rumpfkeil, M. P., and Joo, J. J., "Fluid-Structure Interaction of a Variable Camber Compliant Wing," *53rd AIAA Aerospace Sciences Meeting*, AIAA Paper 2015-1235, Jan. 2015.

[17] Seber, G., and Sakarya, E., "Nonlinear Modeling and Aeroelastic Analysis of an Adaptive Camber Wing," *Journal of Aircraft*, Vol. 47, No. 6, 2010, pp. 2067–2074. doi:10.2514/1.C000312

[18] Murua, J., Palacios, R., and Peiro, J., "Camber Effects in the Dynamic Aeroelasticity of Compliant Airfoils," *Journal of Fluids and Structures*, Vol. 26, No. 4, 2010, pp. 527–543. doi:10.1016/j.jfluidstructs.2010.01.009

[19] Cook, J. R., and Smith, M. J., "Stability of Aeroelastic Airfoils with Camber Flexibility," *Journal of Aircraft*, Vol. 51, No. 6, 2014, pp. 2024–2027. doi:10.2514/1.C032955

[20] Palacios, R., and Cesnik, C. E. S., "Cross-Sectional Analysis of Nonhomogeneous Anisotropic Active Slender Structures," *AIAA Journal*, Vol. 43, No. 12, 2005, pp. 2624–2638. doi:10.2514/1.12451

[21] Kumar, D., and Cesnik, C. E. S., "Performance Enhancement in Dynamic Stall Condition Using Active Camber Deformation," *Journal of the American Helicopter Society*, Vol. 60, No. 2, 2015, pp. 1–12. doi:10.4050/JAHS.60.022001

[22] Abramowitz, M., and Stegun, I. A., *Handbook of Mathematical Functions*, Dover, New York, 1968.

[23] Patil, M. J., and Althoff, M., "Energy-Consistent, Galerkin Approach for the Nonlinear Dynamics of Beams Using Mixed, Intrinsic Equations," *47th AIAA/ASME/ASCE/AHS/ASC Structures, Structural Dynamics, and Materials Conference*, AIAA Paper 2006-1737, May 2006.

[24] Peters, D. A., and Johnson, M. J., "Finite-State Airloads for Deformable Airfoils on Fixed and Rotating Wings," *Proceedings of Symposium on Aeroelasticity and Fluid Structure Interaction Problems, ASME Winter Annual Meeting*, edited by P. P. Friedmann, and J. C. I. Chang, AD—Vol. 44, American Soc. of Mechanical Engineers, New York, 1994, pp. 1–28.

[25] Peters, D. A., Karunamoorthy, S., and Cao, W.-M., "Finite State Induced Flow Models Part I: Two-Dimensional Thin Airfoil," *Journal of Aircraft*, Vol. 32, No. 2, 1995, pp. 313–322. doi:10.2514/3.46718

[26] Su, W., and Cesnik, C. E. S., "Nonlinear Aeroelasticity of a Very Flexible Blended-Wing-Body Aircraft," *Journal of Aircraft*, Vol. 47, No. 5, 2010, pp. 1539–1553. doi:10.2514/1.47317

[27] Bisplinghoff, R., Ashley, H., and Halfman, R., *Aeroelasticity*, Dover, New York, 1996, pp. 532–545.

[28] Theodorsen, T., and Garrick, I. E., "Flutter Calculations in Three Degrees of Freedom," NACA TR-741, 1941.

[29] Zeiler, T. A., "Results of Theodorsen and Garrick Revisited," *Journal of Aircraft*, Vol. 37, No. 5, 2000, pp. 918–920. doi:10.2514/2.2691

M. Smith
*Associate Editor*